**Lea Hehenberger**

# Estimation of Gait Parameters from EEG Source Oscillations

Master Thesis


Institute of Neural Engineering
Laboratory of Brain-Computer Interfaces
Graz University of Technology
Stremayrgasse 16/IV, 8010 Graz, Austria
Head: Univ.-Prof. Dipl.-Ing. Dr.techn. Gernot R. Müller-Putz

Supervisor:
Martin Seeber, Dipl.-Ing.

Evaluator:
Reinhold Scherer, Assoc.Prof. Dipl.-Ing. Dr.techn.

Graz, May 2017

## STATUTORY DECLARATION

I declare that I have authored this thesis independently, that I have not used other than the declared sources / resources, and that I have explicitly marked all material which has been quoted either literally or by content from the used sources.

| | |
|---|---|
| ..... | ..... |
| date | signature |

**Schätzung von Gangparametern aus EEG-Quelloszillationen**

**Zusammenfassung**

**Ziel:** Unter Anwendung eines Modells der kortikalen Repräsentation von aufrechtem Gang sollte während dem Gehen ausgehend von nichtinvasiven EEG-Messungen der Gangzustand (Gehen/Stehen) sowie die Gangfrequenz ermittelt werden. Das betreffende Gangmodell wurde bisher anhand von Analysen von über Gangzyklen gemitteltem EEG, das während roboterunterstütztem Gang aufgezeichnet wurde, dokumentiert. Diese Arbeit übersetzt das Modell für die direkte Anwendung in online-Experimenten.

**Methoden:** Der Gangzustand wird im kortikalen Quellraum aus Wavelet-Amplituden im $\mu$- und$\beta$-Frequenzbereich berechnet, die Gangfrequenz aus denselben im unteren $\gamma$-Bereich berechnet. Ein Verfahren zur Entfernung von Bewegungsartefakten wurde für den Einsatz in Online-Versuchen modifiziert.

**Ergebnisse:** Simulationen mit Daten von roboterunterstütztem Gang brachten gute Ergebnisse für beide Parameter. In Online-Experimenten am Laufband war die Variabilität zwischen Versuchspersonen höher; folglich waren die Ergebnisse weniger zuverlässig.

**Schlussfolgerung:** Es wurde gezeigt, dass Gangparameter in Echtzeit aus dem EEG geschätzt werden können, sofern diese stark genug ausgeprägt sind. Die Ausprägung der zugrunde liegenden Muster variiert beim Gehen am Laufband stark zwischen einzelnen Versuchspersonen.

**Schlüsselwörter:** EEG Quelllokalisation, Gang, neuronale Oszillationen, Zeit-Frequenz-Analyse, Online-Signalverarbeitung

**Estimation of Gait Parameters from EEG Source Oscillations**

**Abstract**

**Objective:** A model of the cortical representation of upright gait was employed to estimate the gate state (walking/standing) and gait cadence (stepping frequency) on the basis of non-invasive EEG recordings. The gait model was previously documented in offline analyses of mean gait cycles in robot-assisted gait.

**Methods:** The gait state is computed in the cortical source space from Wavelet amplitudes in the $\mu$ and $\beta$ frequency bands; the gait cadence is estimated from low $\gamma$ Wavelet amplitudes. A movement artifact correction method was adapted for online use.

**Results:** Simulations on Lokomat data yielded reliable results in both the state identification and the cadence estimation. In online experiments, there was a higher inter-subject variability and lower reliability of the results. Online performance correlated with patterns found in offline analyses.

**Conclusion:** The feasibility of estimating gait parameters from EEG in real time was demonstrated in cases where the underlying patterns where strong enough. During treadmill walking, the strength of these patterns varied strongly between subjects.

**Key words:** EEG source localization, gait, neural oscillations, Time-frequency analysis, online signal processing

# Contents

## Abbreviations

| | |
|---|---|
| **EEG** | Electroencephalogram |
| **ECoG** | Electrocorticogram |
| **ERD/S** | Event-Related Desynchronization/Synchronization |
| **dB** | Decibel |
| **GPM** | Gait Phase related Modulations |
| **WT** | Wavelet Transform |
| **FIR** | Finite Impulse Response |
| **LSL** | Lab Streaming Layer |
| **sLDA** | shrinkage Linear Discriminant Analysis |
| **wMNE** | weighted Minimum Norm Estimates |
| **sLORETA** | standardized Low REsolution brain Electromagnetic TomogrAphy |
| **BEM** | Boundary Element Method |
| **MRI** | Magnet Resonance Imaging |
| **PSCA** | Principal Spectral Component Analysis |
| **MSE** | Mean Squared Error |
| **SNR** | Signal to Noise Ratio |
| **ROI** | Region Of Interest |

Part of this thesis was presented at the 2016 IEEE International Conference on Systems, Man and Cybernetics (SMC) ([21]).

# 1 Introduction

Motor impairments after stroke inhibit affected persons in the performance of basic activities, potentially restricting their daily life. Losing the ability to move freely in one's environment gravely limits one's independence and can have wide-reaching consequences. Rehabilitation should help to limit the burden of long-term impairment and facilitate a large degree of independence. Understanding the underlying cortical processes in healthy persons as well as persons affected by stroke may be a key contributor to the development of efficient novel rehabilitation methods.

In the past, a variety of movement studies employing non-invasive electroencephalography (EEG) and invasive electrocorticography (ECoG) to examine electrocortical activity documented a decrease in $\mu$ (8-13 Hz) and $\beta$ (13-30 Hz) oscillations ([1], [2], [3], [4], [5], [6]), as well as an increase in high $\gamma$ (75-100 Hz) amplitudes ([7]) with respect to a non-movement reference period. The local decrease or increase in neural oscillations of a specific frequency band is a consequence of changes in synchrony of underlying populations of neurons. These changes in synchrony relative to a defined pre-movement baseline are termed Event-Related Desynchronization (ERD) and Event-Related Synchronization (ERS), respectively ([1], [2]).
The cited studies focused on isolated isometric or repetitive movements. A major step on the journey to creating meaningful models of movements to benefit rehabilitation applications as well as the general understanding of the cortical involvement in the facilitation of gait is to move on to more functional types of movements.

In recent years, several studies ([8], [9], [10], [11]) have studied temporal dynamics of EEG signals - in addition to the sustained effects of ERD/S described above - during continuous walking. Contrary to methods like functional Magnet Resonance Imaging, which is extremely sensitive to movement artifacts, and thus only allows for simple, easily controllable isolated movements, EEG is applicable in a mobile setup. Furthermore, EEG has an advantage over methods based on metabolic processes such as functional Near-Infrared Spectroscopy, in that it provides good temporal resolution with regard to the brain activity, making it an apt tool to study movement-related time-varying cortical processes.
[8] investigated EEG during active and passive robot-assisted walking using Independent Component Analysis and equivalent current dipole mapping, and found decreased amplitudes in $\mu$ (8-12 Hz) and $\beta$ (18-21 Hz) oscillations as well as modulations according to the gait phase in the low $\gamma$ (25-40 Hz) frequency range in central midline areas during active walking.
A similar superposition of these effects was identified in [9] during active robot-assisted

gait using Inverse Source Localization ([12], [13], [14], [15]) based on realistic head models with a distributed source model. The relative power decrease in $\mu$ (10-12 Hz) and $\beta$ (18-30 Hz) rhythms on the one hand, and low $\gamma$ (24-40 Hz) modulations on the other were presented as two different aspects of the walking movement.

## 1.1 The Gait Model

This thesis aims at quantifying properties of walking movement represented in cortical activity in real time, building upon the two-element model put forth by [9]:
There, a time-frequency decomposition was performed on the signals of mean gait cycles (gait cycle: interval between two consecutive right heel strikes) in source space. For every mean gait cycle, the relative power was computed, with respect to signals recorded during standing.
ERD reflects a state of cortical excitability in the respective brain areas - in the case of walking: the sensorimotor areas of the neocortex attributed to the legs and feet. Thus, the resulting measurable power decrease in $\mu$ and $\beta$ rhythms can be used as an indicator for a movement state.

Figure 1 illustrates the relative power (in dB) during a mean gait cycle of an exemplary subject (all following illustrative figures show reproduced results). This represents the effect of ERD during movement. The left plot depicts the power spectrum over time, in the left and right paracentral areas. The abscissa denotes the subject specific duration of a mean gait cycle (in this case: 2.078 seconds). The right plot shows the mean power spectrum. The desired features are identified by two distinct negative peaks in the mean power spectrum, in $\mu$ and $\beta$ bands, respectively, whereas peak frequencies and width of the peaks vary between subjects. As demonstrated in the time-frequency plot, the power decrease is sustained throughout the gait cycle. The frequency bands suggested by [9] are highlighted in gray in both plots of figure 1.

On the other hand, amplitude modulations found in the low $\gamma$ (24-40 Hz) ([8],[9]) as well as high $\gamma$ (70-90 Hz) [11] (with the high $\gamma$ modulations' phase inverted with respect to the low $\gamma$ modulation) oscillations reflect the dynamic aspect of the movement. [9] coined the term Gait Phase related Modulations (GPM) for this property.
Figure 2(a) depicts the mean gait cycle modulation pattern exhibited in one subject across the frequency spectrum. This pattern was obtained by removing the temporal mean from the relative power.

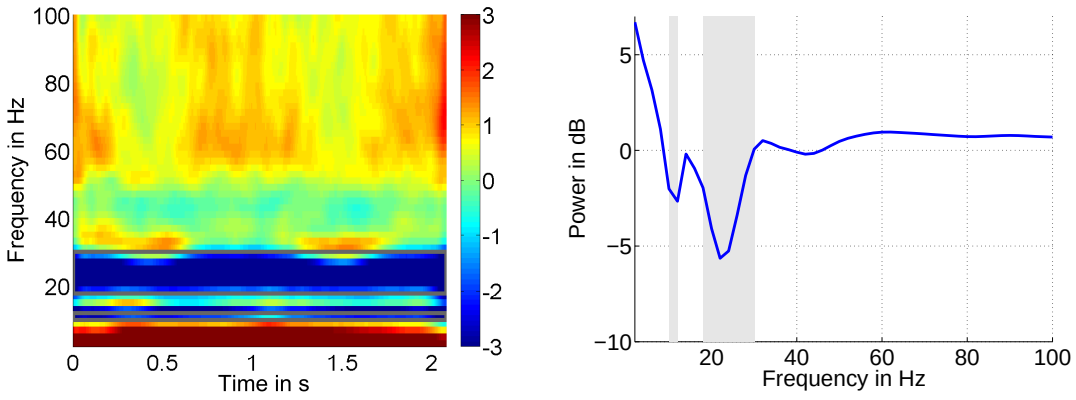


(a) Time-frequency plot (b) Spectrum

Figure 1: Relative power during a mean gait cycle in sensorimotor feet areas (single subject). (a) Relative power spectrum over the duration of one gait cycle, (b) mean relative power spectrum. ERD is expressed in the power decrease in $\mu$ and $\beta$ bands marked in gray.

To quantify the modulating effects across the frequency spectrum, [9] introduced the Gait Phase Modulation (GPM) measure, a complex number indicating to which degree the amplitude of a carrier frequency is modulated according to the gait cadence:

$$GPM(f) = \frac{2}{\sqrt{2} \cdot \sigma_{A(f)} N} \cdot \sum_{n=0}^{N-1} A(n, f) \cdot e^{-2\pi i \frac{2n}{N}} \tag{1}$$

with $f$ and $n$ the respective frequency and time indices, $A$ the magnitude of the time-frequency decomposition, $N$ the number of samples in the cycle, and $\sigma_{A(f)}$ the standard deviation of $A$. In case of perfect sinusoidal modulation with the step frequency, the magnitude of the measure is 1.
The magnitude of the GPM measure across the frequency spectrum for the presented subject is displayed in figure 2(b).
Although there is partial overlap in spatial location and frequency range of the $\beta$ power decrease and the low $\gamma$ modulation, these two phenomena are interpreted to stem from different cortical networks ([9], [16], [17]).
[18] generalized the model to characterize rhythmic movements of both extremities, studying source oscillations during periodic finger movements. The equivalent of GPM was called Movement Phase-related Amplitudes.

In [19], the GPM property was used to reconstruct gait cycle patterns (frequency and phase) from EEG using a Laplace derivation of the Cz position. This was the first instance where the explained model was applied to single-trial data. In a different approach, $\mu$ and $\beta$ power levels were used to identify changes in walking speed during treadmill walking ([20]).

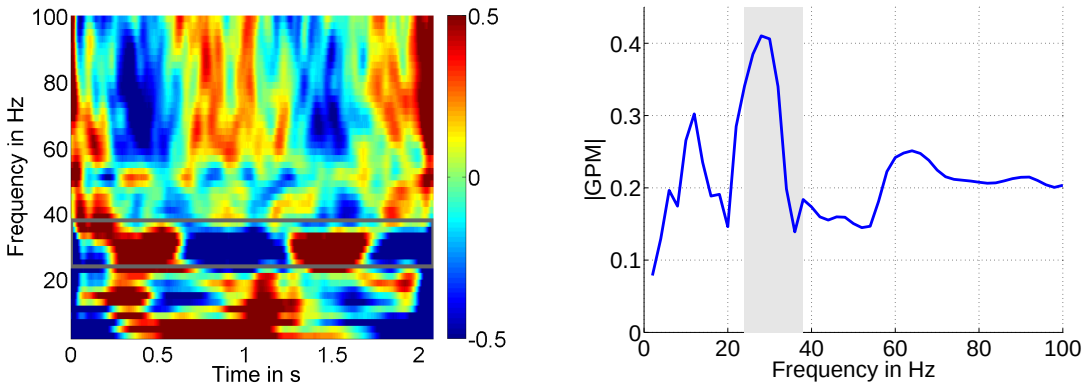


(a) Time-frequency plot of modulation (b) GPM measure

Figure 2: Modulation pattern in a mean gait cycle (single subject). (a) Zero-mean relative power during average gait cycle, (b) Magnitude of the GPM measure across the frequency spectrum.

## 1.2 Objective

This thesis represents an attempt at evaluating the model put forth by [9] online. To this end, an online estimation framework was designed to provide real-time feedback of gait parameters during treadmill walking, employing a two-stage approach: In the first stage, the movement state (movement or stationary) is determined by means of a binary classification of features based on ERD. If a movement state is detected, the gait cadence is estimated using a simple frequency estimation algorithm.

This algorithm looks for the dominant frequency in the Wavelet amplitudes within the low $\gamma$ frequency band (24-38 Hz), which is marked by the gray outlined box in figure 3(a). The mean time course in this frequency band as well as the corresponding amplitude spectrum are presented in figure 3.

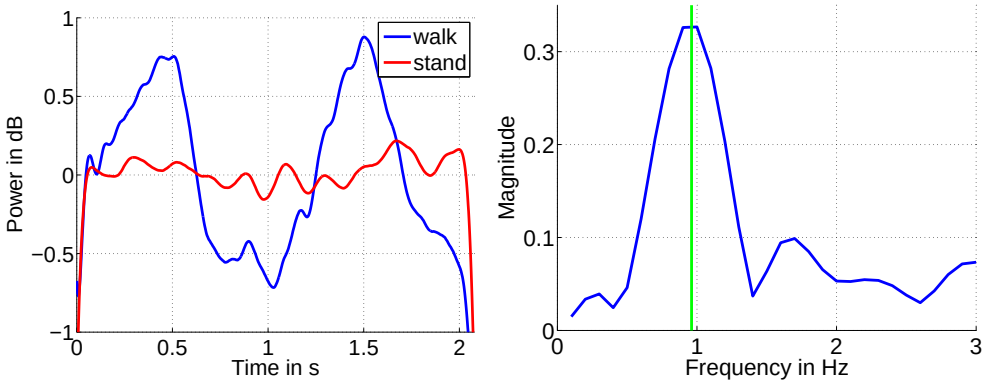


(a) Time course (b) Spectrum

Figure 3: Modulation in the low $\gamma$ frequency band (single subject). (a) Time course, contrasted by the time course during standing in red. (b) Amplitude spectrum (WT). The green line marks the median cadence inferred from heel contact measurements.

## 1.3 Development Process

The development process encompassed two main phases, as illustrated in figure 4: In the first phase, the online data processing and parameter estimation methods were set up. This drafted framework was tested on an offline data set of robot-assisted walking. When promising results were obtained on these data, the framework was implemented for direct online use and applied in three pilot experiments.
The results of phase 1 were presented at the 2016 IEEE International Conference on Systems, Man, and Cybernetics (SMC) ([21]).

After an evaluation of the online results and post-experiment analyses of the recorded EEG, the framework was revised. The revision encompassed parameter adjustments following insights gained from the obtained results of the pilot experiments. Furthermore, an online artifact correction method was implemented.

The revised processing was evaluated on the offline data set, and the pilot recordings. Finally, three additional online experiments were conducted.

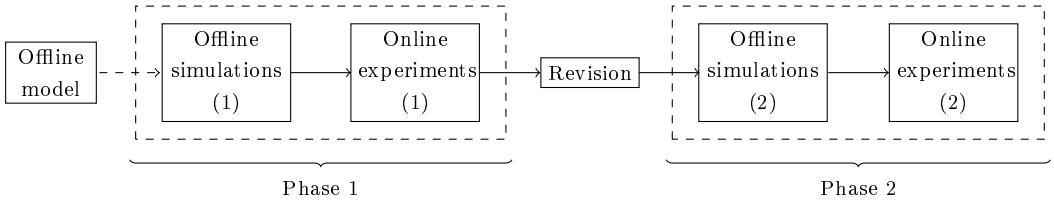


Figure 4: Sketch of the development process.

To my knowledge, this is the first instance where the proposed characterization of gait is applied for online estimation.

# 2 Methods

## 2.1 Gait Parameters

Two sets of features were identified to characterize the gait movement, based on the model put forth in [9], the first of which is used to identify the movement state, and the second to characterize a dynamic component of the movement, i.e. the gait cadence.

Determination of the movement state is treated as a binary classification problem, based on features reflecting the effect of ERD. Said features deviate from the classical definition of ERD, which is computed relatively to a defined reference period before each trial [2]. Being based on continuous walking, the experimental setup does not allow for this.

The gait cadence is estimated by computing the (low-frequent) spectrum of the modulating frequency band, and investigating it for its dominant frequency.

Methods were drafted to extract and process features from live EEG in segments of five seconds at a time. This time window was selected in order to provide feedback at acceptable time intervals, while including several modulation periods.

As sketched in figure 4, before online testing of the designed signal processing framework, its function was validated on an offline data set of 10 healthy subjects walking with the assistance of a Lokomat (Hocoma, Switzerland) robotic gait orthosis. The system was subsequently adapted to actual online use, and applied in online treadmill experiments with three subjects.

After three measurements, the system was subjected to a major revision, including an artifact removal method. The revised processing was again tested on the Lokomat data as well as the data collected in the first three treadmill experiments, before additional experiments were conducted.

## 2.2 Evaluation of Methods on Offline Data

EEG recorded in 10 healthy subjects during walking guided by a Lokomat was chosen as a basis for the development of the signal processing framework, because the patterns from which the features of interest were derived were previously identified in gait cycle averages of the data [9].
Analyses based on the same data set were first published in [8].

In the original experiment, subjects were walking at constant speed, which was determined for each subject according to their respective leg length, varying between 1.8 and 2.2 kph. Participants were instructed to walk naturally without resisting the Lokomat. Originally, three conditions were performed: Active walking (actively supporting the movement trajectory dictated by the Lokomat), passive walking and standing while actively supporting one's body weight. Here, passive walking runs were not included.
EEG recordings were taken at 120 sensor sites using 4 BrainAmp (Brainproducts, Germany) amplifiers. The electrode layout followed the 5% international 10/20 EEG system (EasyCap, Germany) [22]. Ground and reference were placed on the right and left mastoids, respectively. All electrode impedances were made sure to be lower than 10 k$\Omega$.
The true stepping pattern was recorded by means of electro-mechanical pressure sensors fixed to the heels.
Raw data was sampled at 2.5 kHz, subjected to zerophase FIR (Finite Impulse Response)

1 Hz high pass and 200 Hz low pass filters and downsampled to 500 Hz.
The EEG signals were re-referenced to the common average. Channels either superceding 1 mV in amplitude at any time point or with a variance higher than five times the median variance of all channels.

Signal processing and computations were conducted in Matlab (Mathworks, Inc., Natick, USA). After preprocessing, EEG was cut into non-overlapping segments of 5 seconds. If any sample of a segment superceded a threshold of 200 $\mu V$, the segment was omitted.

### 2.2.1 Online Treadmill Experiments

In the online experiments, healthy subjects were walking on a treadmill at low speeds and were instructed to move in a regular periodic manner, keeping the stride length as constant as possible. Furthermore, they were asked to keep their gaze straight ahead and to keep head and shoulder movements to a minimum to limit movement-related artifacts in the EEG.

EEG was recorded with a 64 channel eego$^{TM}$sports system (ANT Neuro, Enschede, Netherlands) at a sampling frequency of 500 Hz. Electrode impedances were less than 20 kΩ. All electrodes including ground and reference electrodes are integrated in the EEG cap. The ground and reference were located at Fpz and CPz, respectively. Four electromechanical pressure sensors (two sensors per foot) were attached to the subjects' heels and balls of the feet, respectively, to record the gait pattern for post-experiment analyses. An overview of the experimental setup is presented in figure 5.

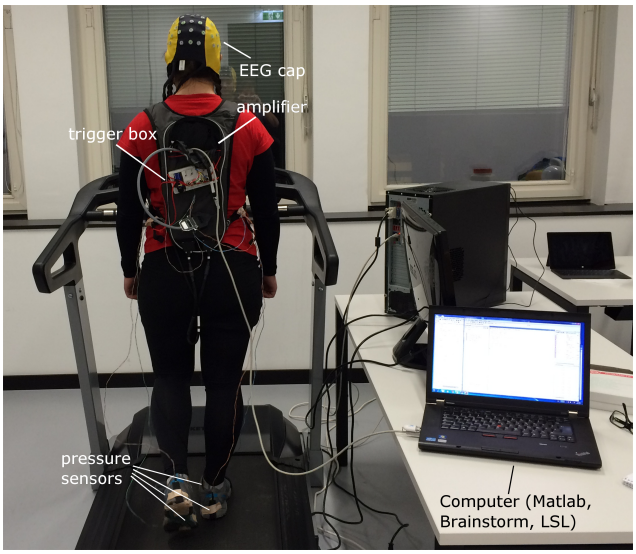


Figure 5: Experimental setup in treadmill experiments. The EEG setup was mobile (EEG cap with integrated electrodes, lightweight amplifier in backpack) and connected to a computer via USB. Pressure sensor signals were transmitted to the amplifier via a custom "trigger box".

Both the EEG and pressure sensor signals were streamed over the network via the Lab Streaming Layer (LSL) [23] framework. Both streams were recorded for use in later offline analyses and troubleshooting purposes. Live EEG was received by Matlab through an LSL inlet, buffered, and then processed in non-overlapping segments of 5 seconds at a time. The core signal processing was identical to the processing applied to the offline data. The preprocessing, on the other hand, had to be applied to each trial segment separately. Raw EEG was subjected to a high-pass filter (4th order Butterworth filter) with a cut-off frequency of 1 Hz. Filter states were saved by the filter object, to avoid swing-in effects.
After the revision of the system, modifications had to be made to reduce computation time, because the new processing could not be conducted within one trial length. To achieve real-time performance, the EEG signals were downsampled (refer to section 2.4 for details).
Channels with high variances were rejected according to the same criteria as for the offline data, and the same amplitude threshold of $200\mu V$ was employed.

The inverse model (see section 2.3) required a noise covariance matrix computed from resting EEG. As in the Lokomat experiments, the non-movement state was defined as upright standing. To this end, a standing period was recorded at the beginning of each experiment. After the revision of the system (phase 2), the same recordings were also used to compute a quasi baseline for trials (see below for details).
Afterwards, training data of the two classes "walking" and "standing" were collected to train the shrinkage Linear Discriminant Analysis (sLDA) classifier. Eventually, evaluation runs with online classification of the gait state as well as estimation of the gait cadence were performed.
Variance based channel rejection was performed according to variances computed from the training runs.

For the first three subjects (phase 1), the treadmill speed remained unchanged throughout the experiment, while in the later experiments (phase 2), different speeds were explored.

## 2.3 Inverse Source Localization

Features were computed in the cortical source space. To this end, inverse source localization was performed to compute sources of cortical activity from non-invasive EEG measurements.
The extracellular potential field measured at EEG electrode locations is essentially said to result from the collective activity of neurons propagated through the so-called volume conductor, i.e. the media surrounding the brain such as the skull and scalp of the head. The

neuronal activity is constituted by a dipole (a source and a sink) of electric current within any neuron experiencing a post-synaptic potential [24]. Inverse source imaging models the causal relationship between neuronal source currents and scalp potentials picked up by EEG sensors as an inverse problem, with the first being the unknown cause and the latter the measured effect.

Inverse source localization was performed with Brainstorm (Tadel et al. 2011), which is documented and freely available for download online under the GNU general public license (http://neuroimage.usc.edu/brainstorm) [25].
The ill-posed inverse problem was modeled by means of a distributed source model, restricting the source space to the cortical surface and the orientation of source dipoles to be perpendicular to the surface.
Source maps were computed using wMNE (weighted Minimum Norm Estimates) ([26]) regularization, and normalized according to sLORETA (Standardized LOw Resolution brain Electromagnetic TomogrAphy) [27].

Forward models were based on realistic head models, computed as layered symmetric Boundary Element Method (BEM) models [28]. To this end, structural T1 MRI scans were recorded with a 3.0 T (Tim Trio/Skyra, Siemens, Erlangen, Germany) scanner and processed using the FreeSurfer analysis suite ([29], [30]), which is documented and freely available for download online (http://surfer.nmr.mgh.harvard.edu/). The forward BEM models themselves were computed in Brainstorm via OpenMEEG [31] [32]. OpenMEEG models four layers, representing the scalp, the inner and outer skull and the cortex.

The resulting inverse model represents a linear mapping from the source space to the sensor space.

The features of interest are expected to be localized in paracentral regions of the cortex, which are ascribed to sensorimotor representation of the lower extremities, and thus were computed from a subset of source vertices in these areas, as defined by the Desikan-Killiany atlas.

## 2.4 Signal Processing and Feature Extraction

### 2.4.1 Time-Frequency Analysis

EEG segments of 5 seconds were subjected to Wavelet decomposition using Morlet Wavelets [33]. The temporal resolution was set to 5 seconds (full width half maximum) at the mother wavelet's center frequency of 1 Hz.
To avoid the influence of edge effects on the feature computation, the time-frequency de-

composition is truncated on both edges in the time dimension.
After the revision, the transformation to the cortical source space took place after the Wavelet transform to reduce computational effort. The time-frequency decomposited signals were mapped as complex signals, and the magnitude subsequently computed in the source space.

### 2.4.2 Feature Extraction (Phase 1)

The feature compuation of phase 1 is illustrated in figure 6.
The input block labeled "Wavelet amplitude" represents the amplitude time courses of the Wavelet transformed signals in source space (averaged across the region of interest), i.e. one time course for each frequency within the defined range (8-40 Hz, in 2 Hz steps).

The classification of the gait state was performed on logarithmic band amplitude features computed from the Wavelet amplitudes in $\mu$ (10-12 Hz) and $\beta$ (22-26 Hz) frequency bands (averaged across the respective frequency bands). The logarithm serves to shape the feature distributions into a more suitable form for the classifier, since LDA classifiers work best on normally distributed data.

For the frequency estimation, the frequency band containing the GPM according to [9] (24-38 Hz) was - after deduction of the temporal mean and averaging across the low $\gamma$ frequency band - again subjected to Wavelet decomposition in the range of 0.1 to 3 Hz, averaged across the temporal dimension, and investigated for its maximum amplitude. The described process is sketched in figure 6.

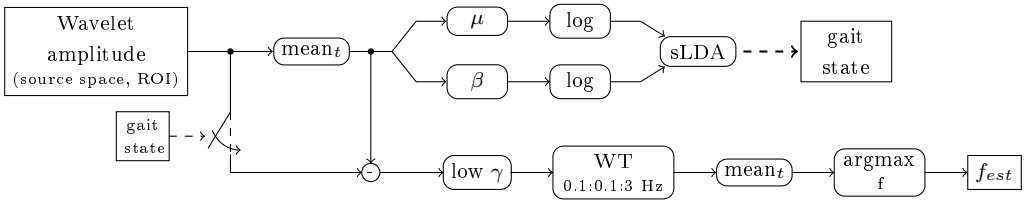


Figure 6: Feature computation (before revision). $ROI$: region of interest, $mean_t$: temporal mean, $\mu$, $\beta$, $low\,\gamma$: extraction of frequency bands and mean over respective bands, $sLDA$: shrinkage LDA classifier, $WT$: Wavelet transform. $argmax_f$: find frequency corresponding to maximum.

### 2.4.3 Feature Extraction (Phase 2)

During the revision, an online artifact correction method was implemented, which is described in section 2.5. The artifact correction method necessitated the computation of the features from the relative Wavelet power (relative to a non-movement baseline) in dB, rather than the Wavelet amplitude.
The standing period recorded to whiten the inverse model's lead field matrix was utilized

to serve as this (quasi) baseline. Moreover, the Wavelet decomposition now had to be conducted over a larger frequency range of 2-100 Hz, and in the whole source space.

Because of the increased compuational load, EEG was downsampled to 250 Hz in the preprocessing stage. After the time-frequency decomposition, the Wavelet transformed time courses were downsampled further, by a factor of 4, resulting in a final sample rate of 62.5 Hz. This is sufficient for the remaining computations, because the first set of features ($\mu$ and $\beta$ band power) does not rely on temporal variation, but rather a sustained power level, and the Gait-Phase related Modulations naturally are low frequent.

The frequency bands for the gait state classification features were expanded to better cover the negative spectral peaks in a broader range of subjects. $\mu$ features were now computed from the frequencies 8-12 Hz, while the $\beta$ range was extended in both directions to 18-30 Hz.

The actual feature computation almost stayed the same as before, with one exception: the logarithmization to reshape the feature distribution for the sLDA classifier was not necessary anymore, because the relative power in dB was already logarithmic.

The revised processing is depicted in figure 7.

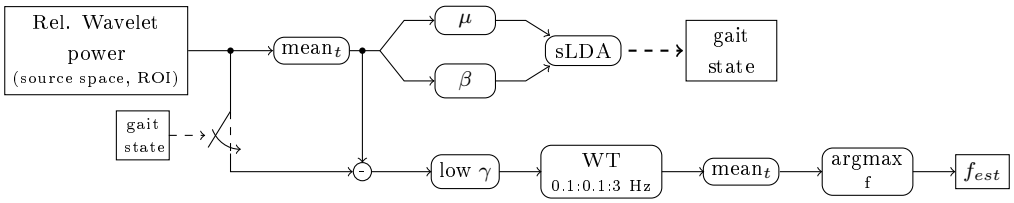


Figure 7: Feature computation (after revision). *ROI*: region of interest, *log*: base 10 logarithm, $mean_t$: temporal mean, $\mu$, $\beta$, $low\,\gamma$: extraction of frequency bands and mean over respective bands, *sLDA*: shrinkage LDA classifier, *WT*: Wavelet transform. $argmax_f$: find frequency corresponding to maximum.

## 2.5 Artifact Treatment

EEG recorded during movement is highly prone to contamination by movement artifacts. To limit the adverse effects on the features, a number of measures were taken.
Subjects were instructed to avoid excess movement, most importantly of the head and shoulders, to limit the effect of artifacts on the EEG signals. However, due to the nature of gait experiments, a certain amount of artifact contamination cannot be avoided.

Trials with strong transient artifacts were discarded via a threshold of $200\mu V$.

Ocular artifacts such as eye blinks are considerably slower than alpha rhythms, and therefore outside of the frequency range used for feature computation. A similar argument can be made for power line artifacts, which occur above the highest frequency of interest for the modulations (38 Hz).

[11] proposed a method to remove movement artifacts, based on Principal Component Analysis in the spectral domain (PSCA). It exploits the fact that muscular artifacts tend to be stronger than EEG and spread over both a broad frequency and spatial range. The time-frequency composed source space signals are subjected to PSCA, and then projected back, discarding the component belonging to the largest eigenvalue of the covariance matrix.
The rejected component was demonstrated to be plausibly consistent with properties associated with movement artifacts - it is spectrally broad-banded and strongest around dorsolateral regions. The features of interest, on the other hand, are all band-limited and spatially confined.

This method was adapted to make it fit for online use, and implemented during the revision. This required major changes to the first draft of the system, where the features where computed only in relevant frequency bands and in source vertices contained in the region of interest.
In order to capture the properties of the artifacts, data is required across a broad frequency spectrum (2-100 Hz) and in the whole source space.

# 3 Results

## 3.1 Phase 1

### 3.1.1 Offline Simulations

#### Gait State

The performance of the gait state classification was evaluated by means of a 10×10 fold cross-validation. The obtained results are summarized in figure 8.

There is a mismatch in the number of trials per class, as well as different amounts of data per subjects. Therefore, a minimum accuracy threshold for better-than-random performance was computed for each subject, with a confidence limit of 0.05.
Accuracies above 83% were achieved, all of them well above the respective thresholds, which range from 55.19% to 66.68%.
Because of the mismatch in trials, the figure is complemented by the sensitivity (true positive rate, i.e. the accuracy of the class "walk") and the specificity (true negative rate,

i.e. the accuracy of the class "stand"). The sensitivity is above 90% for all but one subject and notably higher than the specificity for all subjects.
One subject's specificity does not exceed the threshold, indicating a high false positive rate.

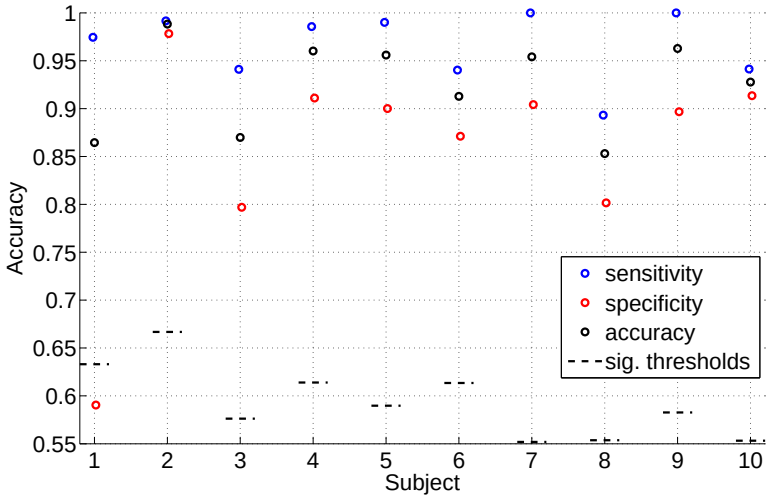


Figure 8: Accuracy, sensitivity and specificity for the 10 subjects in phase 1 of the offline simulation. The dashed line marks subjects' significance thresholds.

To provide some background to these results, the classification features of the trial segments are illustrated in figure 9 by means of scatter plots in the two-dimensional feature space. Visual inspection of the plots reveals that the features are in fact distributed differently for the two classes in all subjects, with considerable variation in the actual distribution between subjects.
In subject 1, a considerable portion of the features of the stationary condition overlap with the features of the walking condition, which accounts for the poor specificity achieved by this subject.
To statistically establish the difference in the distributions, Wilcoxon ranksum tests with a significance level of 0.05 were performed on the sets of $\mu$ and $\beta$ band features. Both sets of features are significantly differently distributed in the two conditions. Table 1 lists the corresponding p-values.

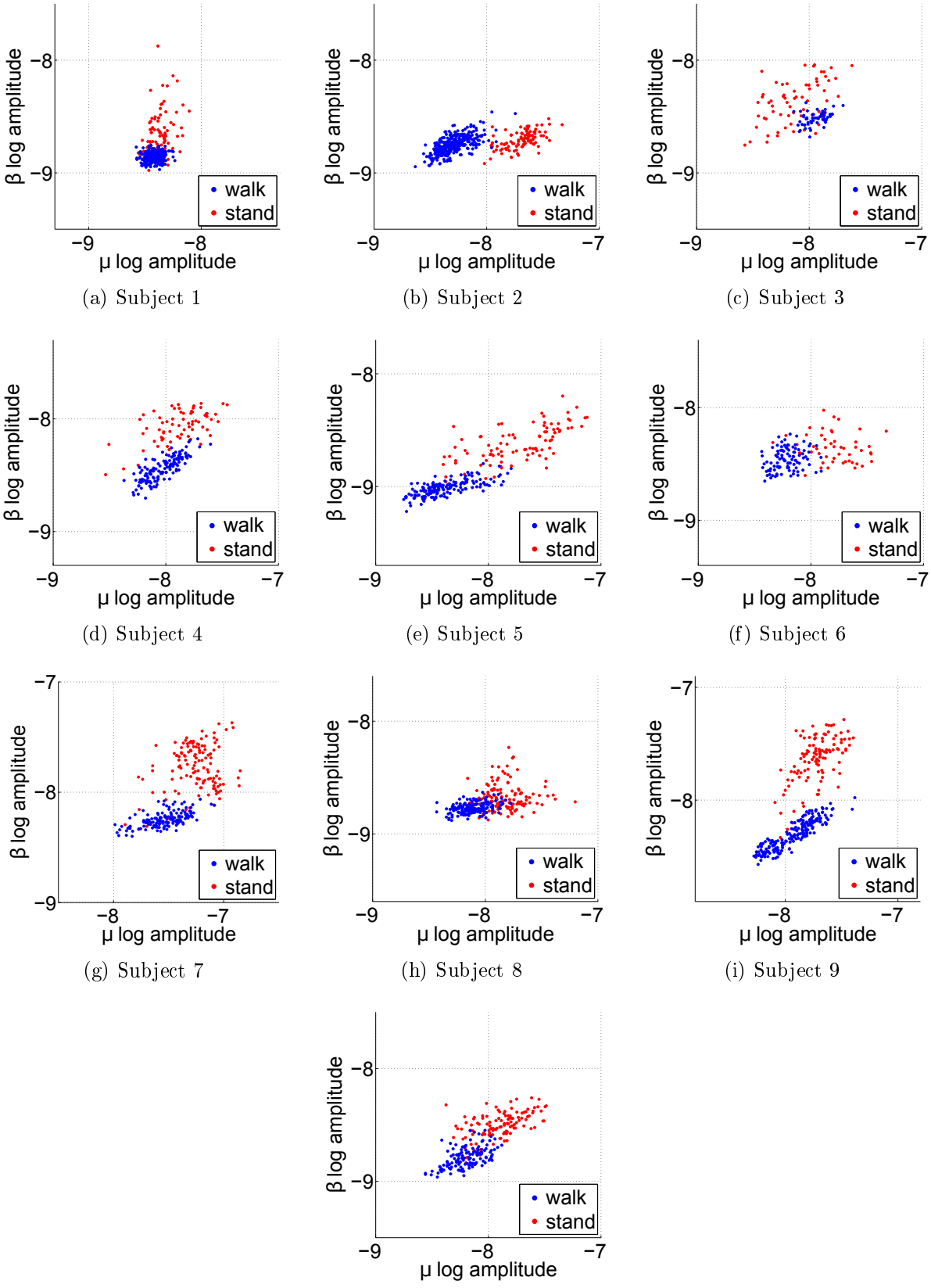


(a) Subject 1 (b) Subject 2 (c) Subject 3

(d) Subject 4 (e) Subject 5 (f) Subject 6

(g) Subject 7 (h) Subject 8 (i) Subject 9

(j) Subject 10

Figure 9: Distribution of logarithmic amplitude features in the two-dimensional feature space (offline simulation, phase 1).

| subject | p-value ($\mu$) | p-value ($\beta$) |
|---|---|---|
| 1 | $8.62 \cdot 10^{-6}$ | $3.75 \cdot 10^{-26}$ |
| 2 | $3.70 \cdot 10^{-53}$ | $4.17 \cdot 10^{-7}$ |
| 3 | $1.22 \cdot 10^{-6}$ | $9.82 \cdot 10^{-6}$ |
| 4 | $4.28 \cdot 10^{-7}$ | $3.06 \cdot 10^{-28}$ |
| 5 | $2.44 \cdot 10^{-31}$ | $3.08 \cdot 10^{-39}$ |
| 6 | $2.31 \cdot 10^{-19}$ | $1.58 \cdot 10^{-5}$ |
| 7 | $8.63 \cdot 10^{-22}$ | $2.32 \cdot 10^{-43}$ |
| 8 | $3.65 \cdot 10^{-33}$ | $2.71 \cdot 10^{-14}$ |
| 9 | $2.35 \cdot 10^{-16}$ | $3.58 \cdot 10^{-44}$ |
| 10 | $7.57 \cdot 10^{-25}$ | $1.95 \cdot 10^{-37}$ |

Table 1: p-values according to ranksum tests on logarithmic amplitude features of the two classes (offline simulation, phase 1).

**Gait Cadence**

The distributions of cadence estimates are illustrated as histograms in figure 10. Because of the different amounts of data per subject and condition, the histograms are normalized by the respective numbers of trials.

The top panels depict the distributions for walking trials, with the median estimate marked in black and a green line at the median true cadence, which was determined from the step intervals defined by the pressure sensor measurements. The bottom panels show the distributions for standing trials; these were computed as a control condition to affirm that the identified modulation frequency is in fact only present in the movement condition and thus a characteristic of the movement dynamics.

For seven subjects, the estimates of walking trials are distributed around the respective median true cadences, i.e. the median estimate lies within one frequency bin around the median true cadence. The best results are obtained in subjects which exhibit strong and highly symmetrical modulation patterns in mean gait cycles (mean patterns are included in the appendix).

The estimates of standing trials show a tendency towards the lower half of the spectrum. To some extent, this property can also be observed in the estimates of walking trials of subjects who do not perform well.

To quantify these differences in distributions between the two conditions, error values were computed as the squared deviation of estimates from the "true" cadence within each trial. The true cadence of a trial was determined from the median of step intervals within the respective trial window. For standing trials, the median true cadence was used.

Wilcoxon ranksum tests (significance level: 0.05) revealed significantly different error distributions in 7 subjects. The ranksum test failures correspond to the subjects with the least accurate estimation results.

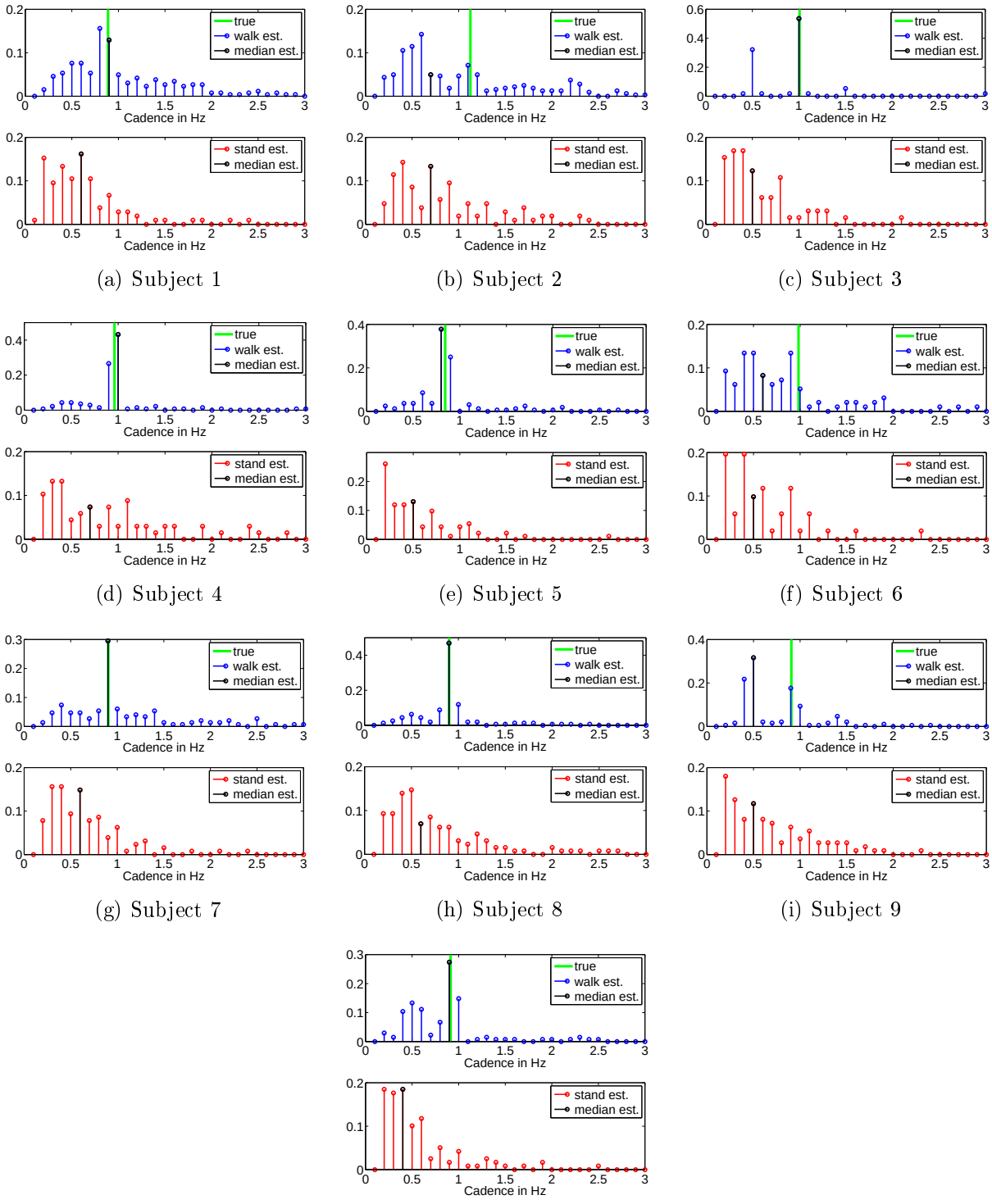


(a) Subject 1 (b) Subject 2 (c) Subject 3

(d) Subject 4 (e) Subject 5 (f) Subject 6

(g) Subject 7 (h) Subject 8 (i) Subject 9

(j) Subject 10

Figure 10: Frequency estimation results of the offline simulation (phase 1). Top panels: Histogram of estimated cadencences for walking trials, weighted by the number of trials. Green lines mark the median true cadences inferred from pressure sensors. Bottom panels: Estimates for standing trials (control condition). Median estimates are accentuated in black.

The p-values, as well as the mean squared error (MSE) values for both conditions are provided in table 2. The MSE values are normalized by the respective numbers of trials for reasons of comparability. For all but one subject, the MSE is higher in the standing condition.

| subject | p-value | MSE (walk) | MSE (stand) |
|---|---|---|---|
| 1 | **0.0958** | 0.0016 | 0.0023 |
| 2 | **0.4592** | 0.0016 | 0.0035 |
| 3 | $7.34 \cdot 10^{-9}$ | 0.0032 | 0.0050 |
| 4 | $8.98 \cdot 10^{-14}$ | 0.0012 | 0.0059 |
| 5 | $2.62 \cdot 10^{-14}$ | 0.0011 | 0.0034 |
| 6 | **0.5746** | 0.0035 | 0.0059 |
| 7 | $4.29 \cdot 10^{-3}$ | 0.0033 | 0.0017 |
| 8 | $2.62 \cdot 10^{-15}$ | 0.0011 | 0.0027 |
| 9 | $7.23 \cdot 10^{-5}$ | 0.0009 | 0.0024 |
| 10 | $3.42 \cdot 10^{-11}$ | 0.0014 | 0.0025 |

Table 2: p-values resulting from ranksum tests performed on the distributions of the squared deviations from the median cadence, and mean squared errors for both conditions. MSE values are normalized by numbers of trials. Bold numbers mark non-significant differences.

### 3.1.2 Online Treadmill Experiments

Figure 11 depicts the results of a $10 \times 10$ fold cross-validation of the gait state classification on the signals recorded in the first three treadmill experiments.
Subject 1 achieved comparable accuracy to the Lokomat subjects. While subject 3 still performed decidedly better than chance, subject 2's accuracy is barely 5% above the threshold. In all three subjects, the sensitivity and specificity are within a $\pm 5\%$ margin of the respective accuracies.

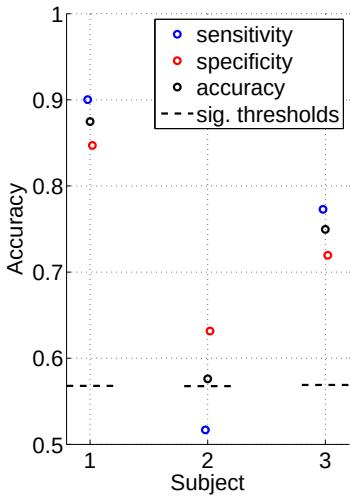


Figure 11: Accuracy, sensitivity and specificity for the 3 subjects in the first phase of online experiments. The dashed line marks subjects' significance thresholds.

Figure 12 depicts the logarithmic amplitudes features in the feature space. The feature distributions of the two conditions are distinct in subject 1 and - albeit to a lesser degree - subject 3. In subject 3, the distributions differ in variance, but strongly overlap.

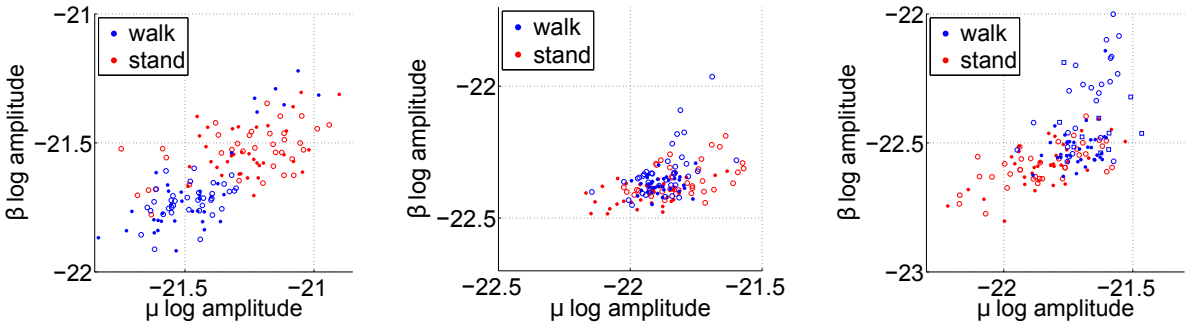


(a) Subject 1 (b) Subject 2 (c) Subject 3

Figure 12: Distribution of logarithmic amplitude features in the two-dimensional feature space (online experiments, phase 1). Individual runs are identified by different markers: Dots mark training runs, circles and squares mark evaluation runs.

According to Wilcoxon ranksum tests performed on the classification features, there is a significant difference between the two conditions in both sets of features for subjects 1 and 3, and in the $\beta$ band features for subject 2. The p-values are provided in table 3.

### Gait Cadence

The estimation results are summarized in the form of weighted histograms in figure 13, in the same manner as the results of the offline simulation. Subject 1 shows a gross estimation bias towards a lower frequency, greatly overshadowing the correct estimates. In

| subject | p-value ($\mu$) | p-value ($\beta$) |
|---|---|---|
| 1 | $1.80 \cdot 10^{-10}$ | $4.55 \cdot 10^{-15}$ |
| 2 | **0.5745** | $7.74 \cdot 10^{-3}$ |
| 3 | $4.93 \cdot 10^{-10}$ | $9.81 \cdot 10^{-11}$ |

Table 3: p-values according to ranksum tests on logarithmic amplitude features of the two conditions (online experiments, phase 1). The bold number marks a non-significant difference.

subjects 2 and 3, the median estimate underestimates the cadence by approximately 0.4 Hz. The variance is high, especially in subject 2. Furthermore, the same trend towards the lower end of the spectrum, which was noted above, can be observed in estimates of the standing condition, as well as the walking condition for subjects 2 and 3.

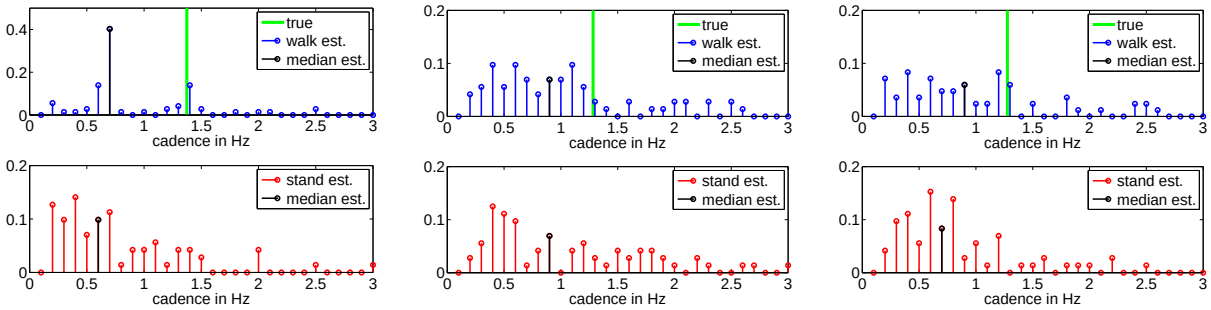


(a) Subject 1 (b) Subject 2 (c) Subject 3

Figure 13: Frequency estimation results of pilot online experiments. Top panels: Histogram of estimated cadencences for walking trials, weighted by the number of trials. Green lines mark the median true cadences. Bottom panels: Estimates for standing trials (control condition). Median estimates are acccentuated in black.

As a consequence, the squared deviations from the mean cadences are similarly distributed in both conditions in the latter 2 subjects, and the corresponding ranksum tests fail. In subject 1, the error distributions are significantly different.
Table 4 shows the p-values and MSEs. All MSEs are higher than in the offline simulations.

| subject | p-value | MSE (walk) | MSE (stand) |
|---|---|---|---|
| 1 | $1.01 \cdot 10^{-2}$ | 0.0067 | 0.0096 |
| 2 | **0.5395** | 0.0094 | 0.0108 |
| 3 | **0.6610** | 0.0094 | 0.0066 |

Table 4: p-values resulting from ranksum tests performed on the distributions of the squared deviations from the median cadence, and mean squared errors for both conditions (online experiments, phase 1). MSE values are normalized by the numbers of trials. Bold numbers mark non-significant differences.

## 3.2 Phase 2

### 3.2.1 Offline Simulation

#### Gait State

All subjects achieved an accuracy greater than 85%, with all but two higher than 90%. The sensitivity is higher than the overall accuracy for all subjects. For subjects 1, 3 and 8 the specificity has improved by approximately 10% and more, compared to phase 1. All values are above the significance thresholds.
Cross-validated accuracies, sensitivities and specificities are depicted in figure 14.

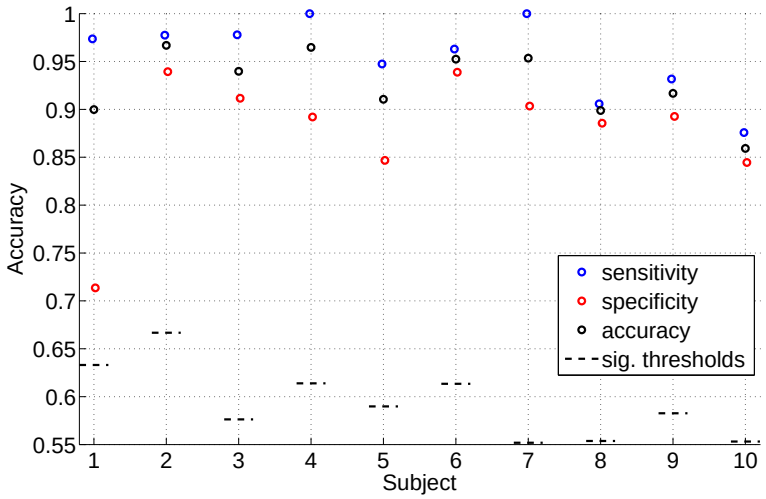


Figure 14: Accuracy, sensitivity and specificity for the 10 subjects in phase 2 of the offline simulation. The dashed line marks subjects' significance thresholds.

Figure 15 depicts the $\mu$ and $\beta$ band power features in the feature space. Compared to the logarithmic amplitude features used in phase 1 (figure 9), the distributions are slightly rotated, and in some subjects, the separability has improved, but the shape of the distributions did not change fundamentally.

For subject 1 and 4, the $\mu$ band features are not significantly different. There is, however, a significant difference in the $\beta$ band features in both cases. This is in accord with the feature distributions shown in figure 15(a) and 15(d), respectively. Table 5 provides the corresponding p-values.

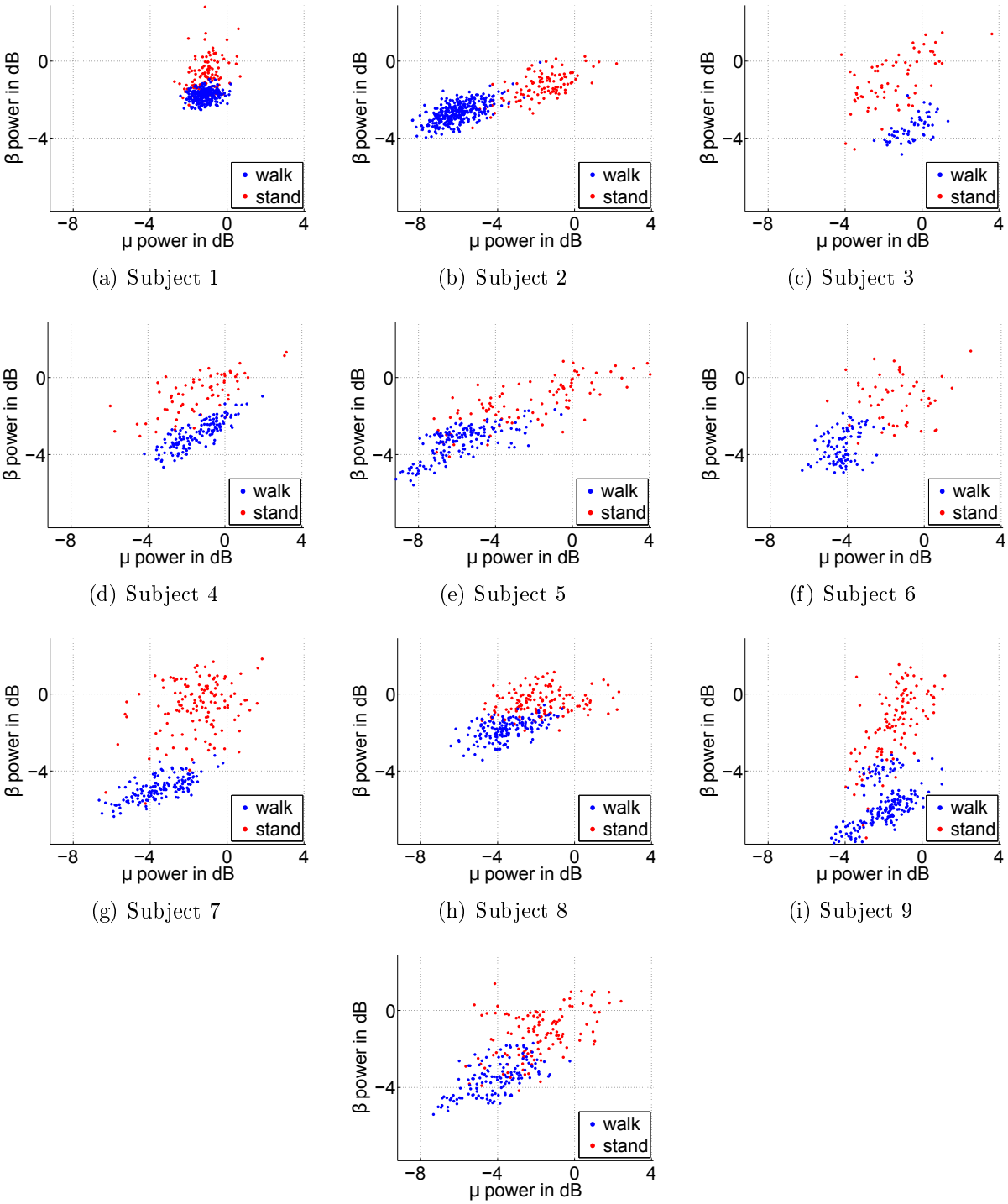


(a) Subject 1 (b) Subject 2 (c) Subject 3

(d) Subject 4 (e) Subject 5 (f) Subject 6

(g) Subject 7 (h) Subject 8 (i) Subject 9

(j) Subject 10

Figure 15: Distribution of band power features in the two-dimensional feature space (offline simulation, phase 2).

| subject | p-value ($\mu$) | p-value ($\beta$) |
|---|---|---|
| 1 | **0.0632** | $1.23 \cdot 10^{-35}$ |
| 2 | $6.15 \cdot 10^{-52}$ | $1.73 \cdot 10^{-41}$ |
| 3 | $1.07 \cdot 10^{-4}$ | $1.19 \cdot 10^{-17}$ |
| 4 | **0.4534** | $5.67 \cdot 10^{-25}$ |
| 5 | $5.09 \cdot 10^{-22}$ | $1.18 \cdot 10^{-30}$ |
| 6 | $1.06 \cdot 10^{-19}$ | $1.60 \cdot 10^{-19}$ |
| 7 | $3.98 \cdot 10^{-23}$ | $2.07 \cdot 10^{-44}$ |
| 8 | $1.02 \cdot 10^{-20}$ | $2.14 \cdot 10^{-42}$ |
| 9 | $1.26 \cdot 10^{-4}$ | $8.23 \cdot 10^{-41}$ |
| 10 | $1.03 \cdot 10^{-20}$ | $2.01 \cdot 10^{-32}$ |

Table 5: p-values according to ranksum test of power features of the two classes (offline simulation, phase 2). Bold numbers mark non-significant differences.

**Estimation of the Gait Cadence**

Histograms of the cadence estimates for both conditions are depicted in figure 16. For five subjects, the revised methods improved the estimation result. All median estimates of the walking condition are now within one frequency bin of the median true cadence. In some cases, the variance is still rather high. These cases correspond to weak or irregular modulation patterns in mean gait cycles. Estimates of standing trials are more flatly distributed than before.

Concerning the MSEs, there is little change compared to phase 1. In the three subjects with non-significant differences in the error distributions in phase 1, the difference remains non-significant. In addition, subject 7's walking error distribution is not significantly different from the standing error distribution, which can be attributed to a shift in the distribution of standing trial estimates.

| subject | p-value | MSE (walk) | MSE (stand) |
|---|---|---|---|
| 1 | **0.4194** | 0.0015 | 0.0021 |
| 2 | **0.1415** | 0.0011 | 0.0030 |
| 3 | $6.19 \cdot 10^{-7}$ | 0.0029 | 0.0042 |
| 4 | $5.60 \cdot 10^{-8}$ | 0.0012 | 0.0057 |
| 5 | $3.75 \cdot 10^{-12}$ | 0.0011 | 0.0024 |
| 6 | **0.2839** | 0.0030 | 0.0052 |
| 7 | **0.2843** | 0.0024 | 0.0016 |
| 8 | $5.12 \cdot 10^{-8}$ | 0.0012 | 0.0021 |
| 9 | $1.97 \cdot 10^{-2}$ | 0.0012 | 0.0027 |
| 10 | $4.48 \cdot 10^{-13}$ | 0.0009 | 0.0028 |

Table 6: p-values resulting from ranksum tests performed on the distributions of the squared deviations from the median cadence, and mean squared errors for both conditions (offline simulation, phase 2). MSE values are normalized by the numbers of trials. Bold p-values mark non-significant differences.

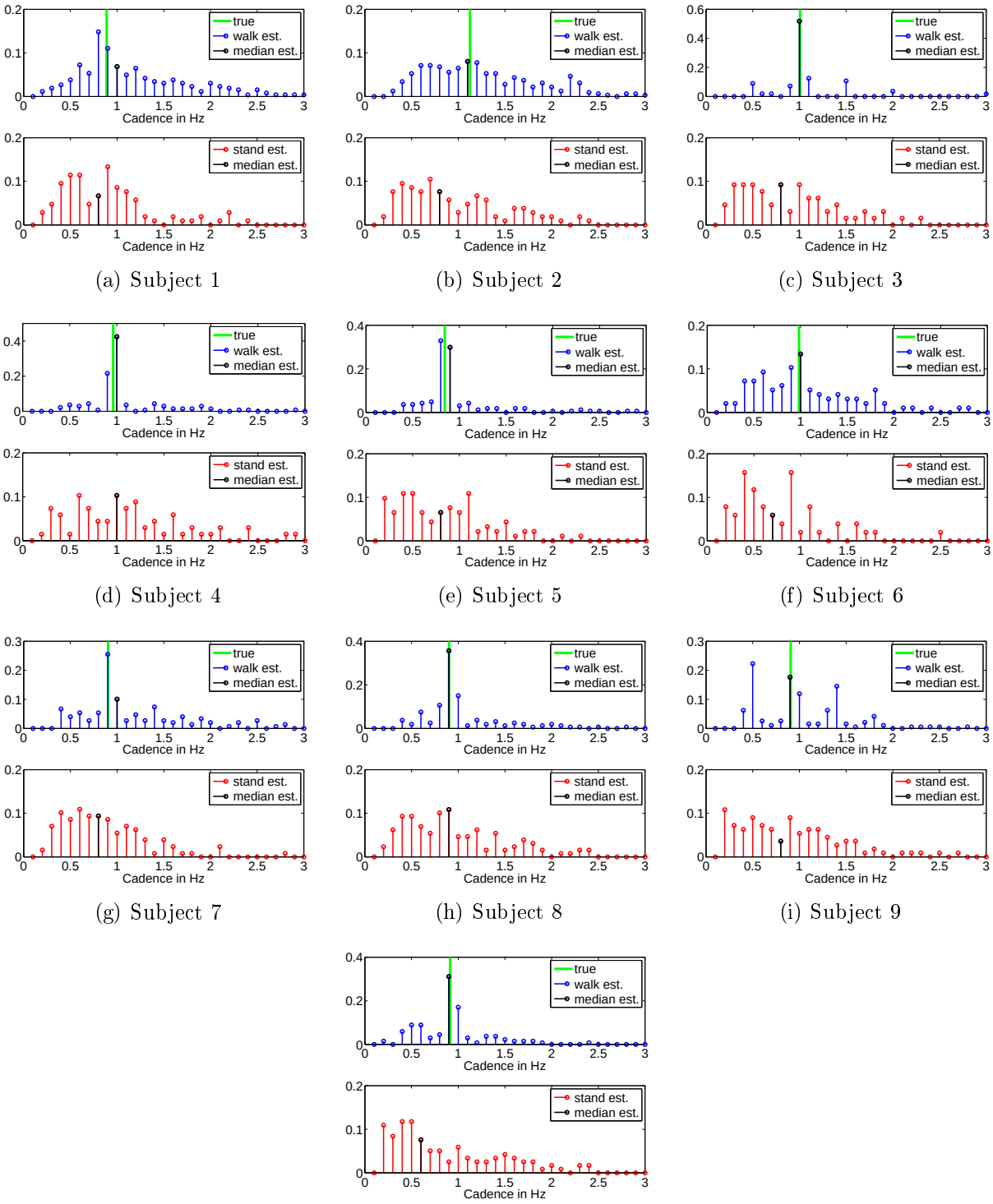


(a) Subject 1 (b) Subject 2 (c) Subject 3

(d) Subject 4 (e) Subject 5 (f) Subject 6

(g) Subject 7 (h) Subject 8 (i) Subject 9

(j) Subject 10

Figure 16: Frequency estimation results of offline simulation (phase 2). Top panels: Histogram of estimated cadencences for walking trials, weighted by the number of trials. Green lines mark the median true cadences. Bottom panels: Estimates for standing trials (control condition). Median estimates are accentuated in black.

### 3.2.2 Re-Evaluation of Treadmill Pilots and Further Online Experiments

#### Gait State

Figure 17 depicts the cross-validated results of the gait state classification using the revised processing for the three subjects introduced in section 3.1.2 and three additional subjects. The figure is complemented by the same performance metrics for just the training data, in square markers. The corresponding significance thresholds for the training data are presented in gray.

Subjects 3, 5 and 6 perform more than 10% worse in the cross-validated classification of all recorded data, than if only the training runs are used. In the case of subjects 5 and 6, the overall accuracies fall below the significance thresholds. Therefore, the accuracies, sensitivities and specificities obtained from a cross-validation of the training data are added to figure 17 in square markers. The disparity of the two significance thresholds for subject 5 is due to a higher mismatch between walking and standing trials in the whole data set, in contrast to the training data.

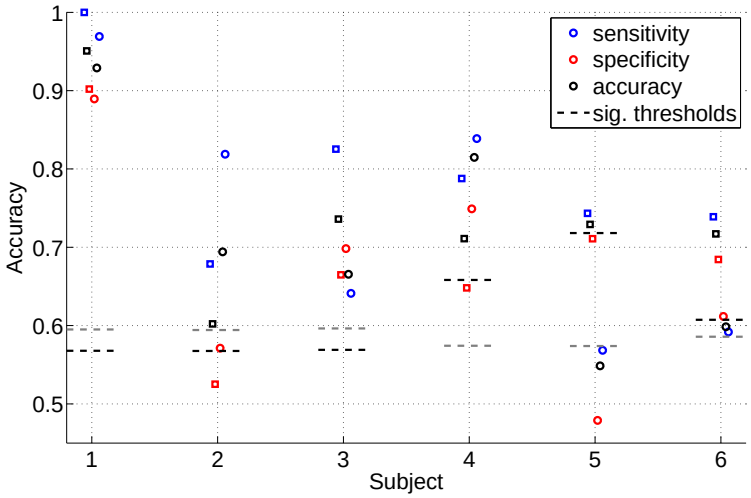


Figure 17: Accuracy, sensitivity and specificity for the re-evaluation of the first 3 treadmill subjects and the online experiments of the latter three subjects. The dashed black line marks subjects' significance thresholds. Square markers depict the respective values when excluding the evaluation runs, with the dashed grey line the corresponding threshold.

The power features of the first three subjects are illustrated in feature space in figure 18. Evidently, the separability of the distributions has improved for subject 1, which accounts for an embellishment of the performance measures. Subject 2's distributions have shifted, but still overlap strongly. The standing features are more spread, which leads to the slight embellishment of the accuracy. Contrarily, subject 3 performed worse than before. Inspection of figure 18(c) suggests that this is a consequence of a downward shift of the walking distribution relative to the standing distribution.

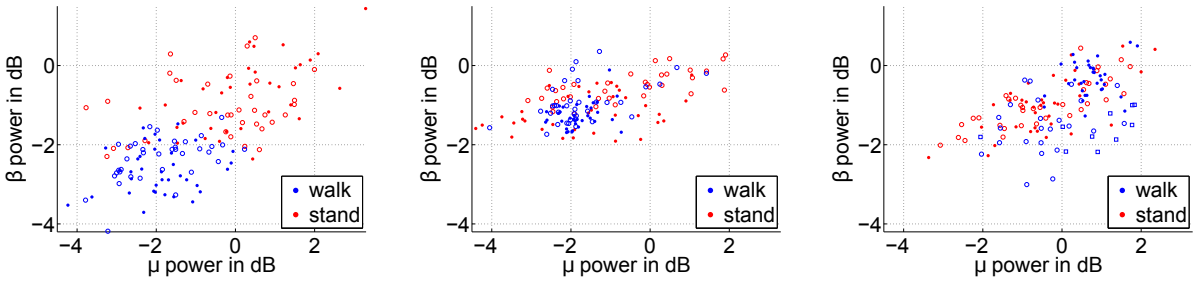


(a) Subject 1 (b) Subject 2 (c) Subject 3

Figure 18: Distribution of band power features in the two-dimensional feature space (re-evaluation of online subjects 1-3). Runs are identified by different markers: Dots mark training runs, circles and squares mark evaluation runs.

Figure 19 displays the features of subjects 4, 5 and 6. For subjects 5 and 6, there is a crass change in the distributions between training runs and evaluation runs. To clearly depict these data, the band power features of the training runs are shown in the top panels, and those of all runs in the bottom panels.

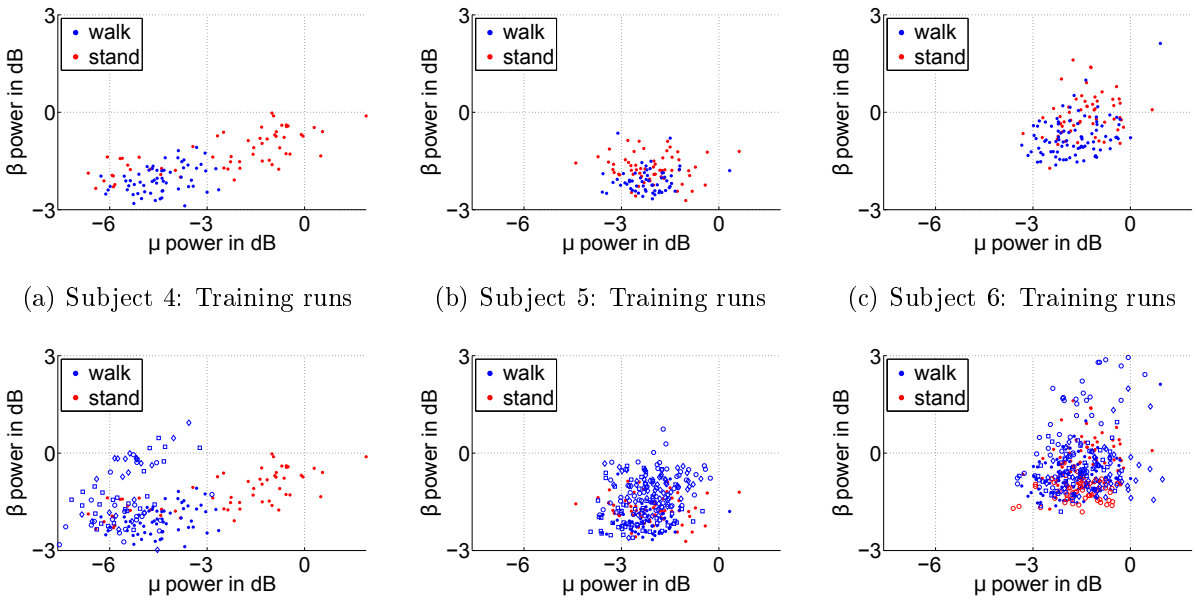


(a) Subject 4: Training runs (b) Subject 5: Training runs (c) Subject 6: Training runs

(d) Subject 4: All runs (e) Subject 5: All runs (f) Subject 6: All runs

Figure 19: Distribution of band power features in feature space (online experiments, subjects 4-6). (a)-(c) Training runs only, (d)-(f) all runs. Runs are identified by different markers: Dots mark training runs, circles, squares and diamonds mark evaluation runs.

According to Wilcoxon ranksum tests, in subjects 1, 2 and 4, there is a significant difference in both band power features. In subjects 3 and 6, there is a significant difference in one feature (subject 3: $\beta$, subject 6: $\mu$).

Because of the feature distribution shift between training and evaluation runs in some subjects, ranksum tests were additionally performed on the training data, for comparison. In all but one of those cases, the difference is significant in the training data.
The p-values are listed in table 7, with the p-values for training runs in brackets.

| subject | p-value ($\mu$) | p-value ($\beta$) |
|---|---|---|
| 1 | $7.58 \cdot 10^{-13}$ | $7.60 \cdot 10^{-21}$ |
| 2 | $1.70 \cdot 10^{-3}$ | $2.54 \cdot 10^{-3}$ |
| 3 | $1.07 \cdot 10^{-4}$ | **0.4803** ($3.20 \cdot 10^{-5}$) |
| 4 | $6.79 \cdot 10^{-13}$ | $2.45 \cdot 10^{-4}$ |
| 5 | **0.5287** (**0.4144**) | **0.0649** ($4.38 \cdot 10^{-7}$) |
| 6 | **0.2062** ($1.05 \cdot 10^{-2}$) | $3.50 \cdot 10^{-3}$ |

Table 7: p-values according to ranksum test of power features of the two conditions (treadmill experiments, phase 2). Bold numbers mark non-significant differences. (in brackets: p-values for training data)

### $\mu$ and $\beta$ Power in Average Gait Cycle

Figures 20 and 21 depict the relative power in the region of interest during a mean gait cycle, for subjects 1-3 and subjects 4-6, respectively. Top panels show time-frequency plots and bottom panels the power spectra. For reasons of comparability, all colorscales and axes in the mean gait cycle plots are set to the same scales as in the corresponding plots in figures 1 and 2.
The strength and frequency locations of the spectral $\mu$ and $\beta$ peaks provide possible explanations for the classification performance of the subjects. In the case of subject 1, both frequency peaks are covered well enough by the frequency bands used for feature computation. Subject 2's $\mu$ peak is very narrow, and the $\beta$ peak very weak and located a little below the defined $\beta$ band. In subject 3, the $\mu$ peak is almost negligible, while the $\beta$ power decrease is not sustained throughout the (mean) gait cycle. This may result from an overlap with the GPM in this frequency band.

Subject 4 exhibits pronounced sustained power decrease in both the $\mu$ and $\beta$ band. Subjects 5 and 6, on the other hand, show very weak patterns. In addition, subject 6 shows an unusual power increase in the upper half of the $\beta$ band.

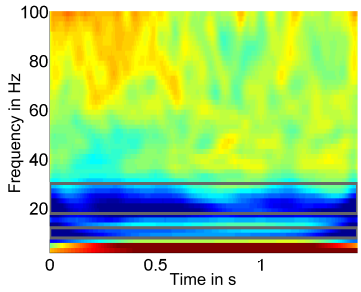


(a) Relative power time-frequency plot (in dB)

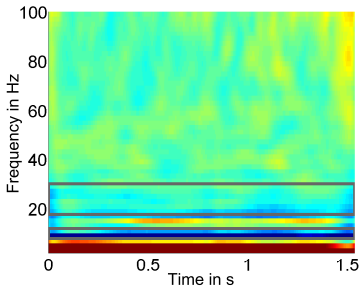


(b) Relative power time-frequency plot (in dB)

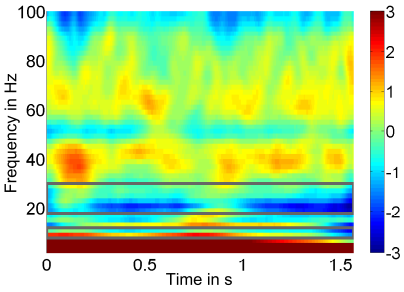


(c) Relative power time-frequency plot (in dB)

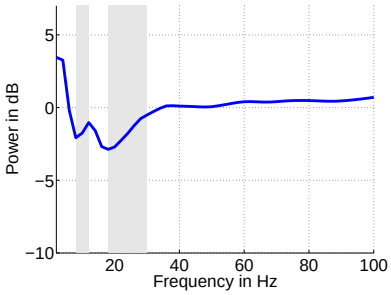


(d) Relative power spectrum

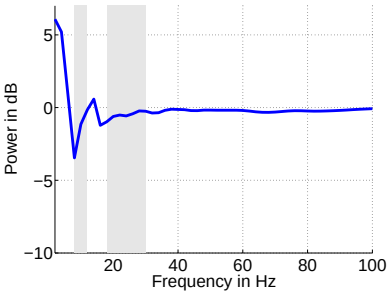


(e) Relative power spectrum

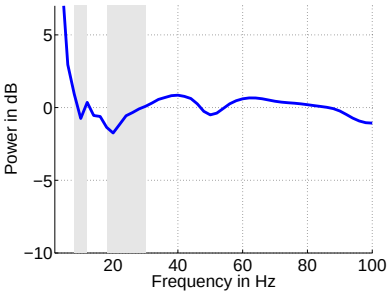


(f) Relative power spectrum

Figure 20: Relative power during a mean gait cycle in ROI (treadmill experiments, subjects 1, 2, 3). The grey outlined boxes in (a)-(c) and grey shadowed areas in (d)-(f) mark the frequency bands chosen for feature computation.

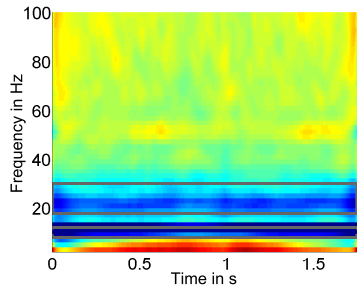


(a) Relative power time-frequency plot (in dB)

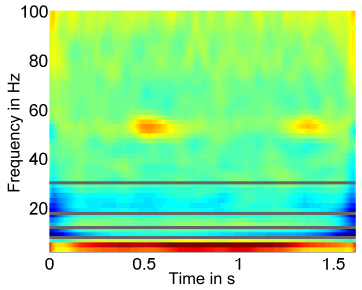


(b) Relative power time-frequency plot (in dB)

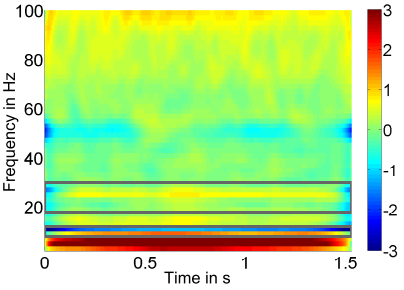


(c) Relative power time-frequency plot (in dB)

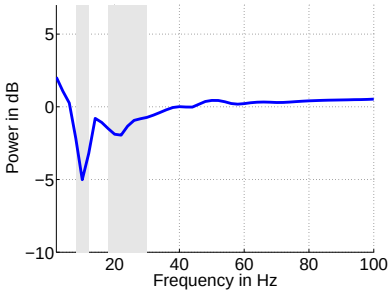


(d) Relative power spectrum

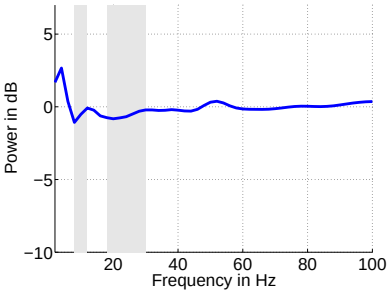


(e) Relative power spectrum

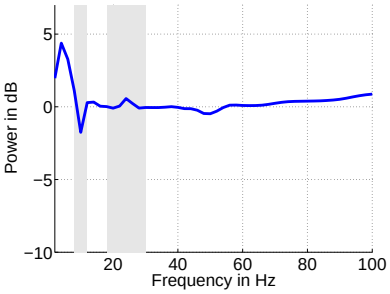


(f) Relative power spectrum

Figure 21: Relative power during a mean gait cycle in ROI (treadmill experiments, subjects 4, 5, 6). The grey outlined boxes in (a)-(c) and grey shadowed areas in (d)-(f) mark the frequency bands chosen for feature computation.

### Estimation of the Gait Cadence

Figure 22 depicts histograms of the cadence estimates for subjects 1, 2 and 3.
Compared to phase 1 (see figure 13), the results have improved. While the estimates are still not satisfactory, the estimation bias of subject 1 has decreased, and for subjects 2 and 3, the median estimate is within 2 frequency bins of the median true cadence, and the variance has decreased.

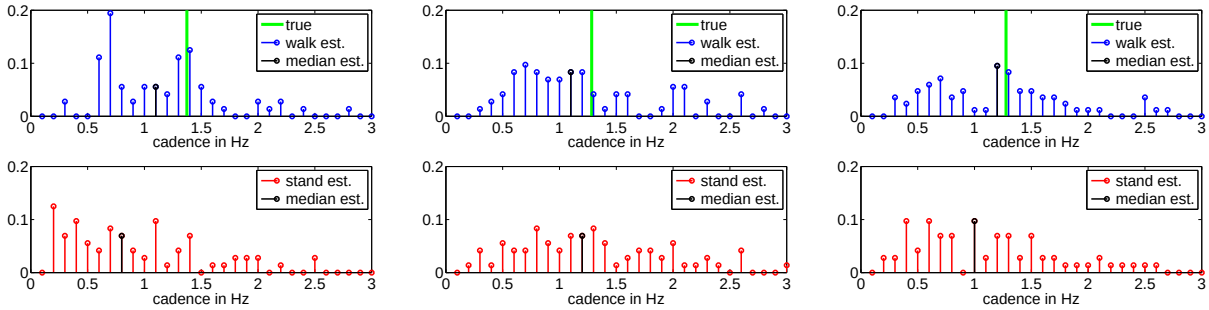


(a) Subject 1 (b) Subject 2 (c) Subject 3

Figure 22: Frequency estimation results of simulations of the revised system (subjects 1, 2, 3). Top panel: Histogram of estimated cadencences for walking trials, weighted by the number of trials. Green lines mark the true cadences as measured by sensors. Bottom panel: Estimates for standing trials (control condition). Median estimates are accentuated in black.

Figure 23 shows the histograms for subjects 4, 5 and 6. For each of these subjects, the treadmill speed was varied between two speeds. The estimates corresponding to the respective lower speeds are depicted in the top panels.
For subjects 4 and 5, the median estimate of the walking condition is within one bin of the median true cadence. However, there is a high degree of randomness, especially in speed 1 of subject 4. Curiously, he standing estimates of subjects 4 and 5 are not flatly distributed, but rather trend towards a dominant frequency. In the case of subject 6, all conditions result in a similar distribution, which is centered around 0.5 Hz.

According to ranksum tests, the squared errors of all subjects but the first one are not significantly different in walking and standing conditions.
The MSE of the walking condition is lower than that of the standing condition in all cases except two: subjects 4 and 6, both in the faster walking condition.

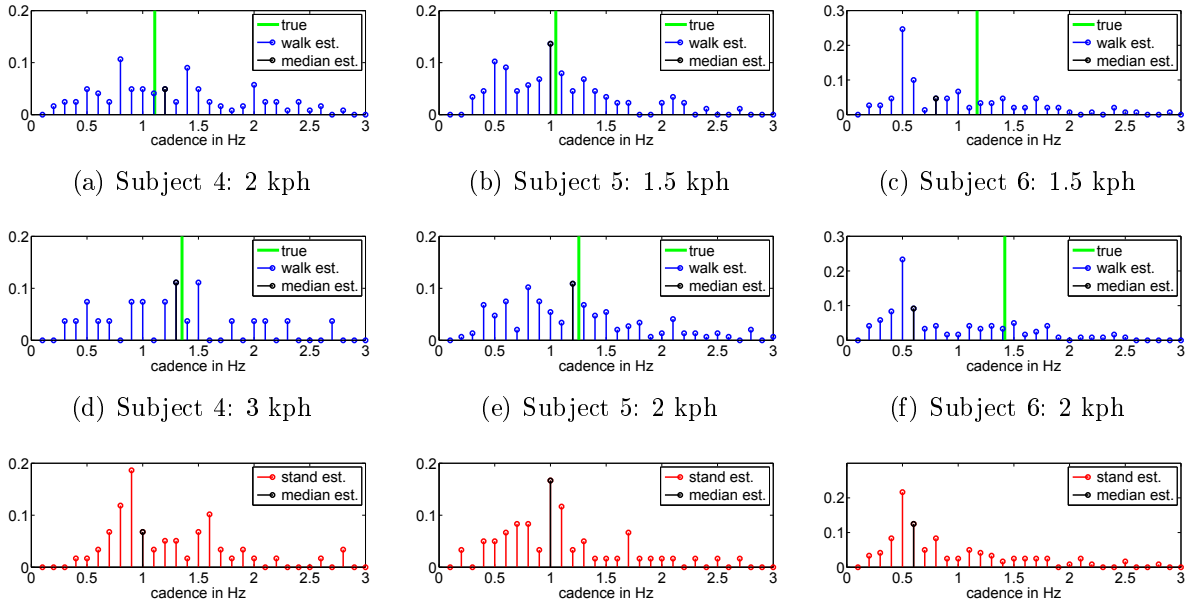


(a) Subject 4: 2 kph (b) Subject 5: 1.5 kph (c) Subject 6: 1.5 kph

(d) Subject 4: 3 kph (e) Subject 5: 2 kph (f) Subject 6: 2 kph

(g) Subject 4: standing (h) Subject 5: standing (i) Subject 6: standing

Figure 23: Frequency estimation results of online experiment (subjects 4, 5, 6). Top and middle panels: Weighted histogram of estimated cadences for speed 1 and 2, resp. Green lines mark the true cadences as measured by sensors. Bottom panels: Estimates for standing trials (control condition). Median estimates are accentuated in black.

| | speed 1 | | | speed 2 | | |
|---|---|---|---|---|---|---|
| subject | p-value | MSE (walk) | MSE (stand) | p-value | MSE (walk) | MSE (stand) |
| 1 | $1.09 \cdot 10^{-3}$ | 0.0044 | 0.0081 | - | - | - |
| 2 | **0.8183** | 0.0054 | 0.0057 | - | - | - |
| 3 | **0.2114** | 0.0052 | 0.0055 | - | - | - |
| 4 | **0.1327** | 0.0037 | 0.0051 | **0.3924** | 0.0121 | 0.0052 |
| 5 | **0.8132** | 0.0031 | 0.0049 | **0.9827** | 0.0025 | 0.0053 |
| 6 | **0.9821** | 0.0084 | 0.0099 | **0.2280** | 0.0156 | 0.0149 |

Table 8: p-values resulting from ranksum tests performed on the distributions of the squared deviations from the median cadence (online experiments, phase 1). MSE values are normalized by the numbers of trials. Bold p-values mark non-significant differences.

### Modulation Pattern in Average Gait Cycle

Figure 24 illustrates the modulation patterns in a mean gait cycle for the first three subjects. The leftmost panels depict the time-frequency plot of the relative power in a mean gait cycle, with the temporal mean removed. The second column shows the magnitude of the GPM measure across the frequency spectrum. The right plots display the time course and the low-frequent amplitude spectrum of the low $\gamma$ frequency band marked in the left plots.

The time signal and the amplitude spectrum of the frequency band with the highest GPM peak is added to the respective plots, identified by dashed black lines - with the exception of subject 1, where adjustig the frequency band does not produce different results. Estimation results in case of subject-specific frequency bands according to GPM peaks are presented in the appendix.

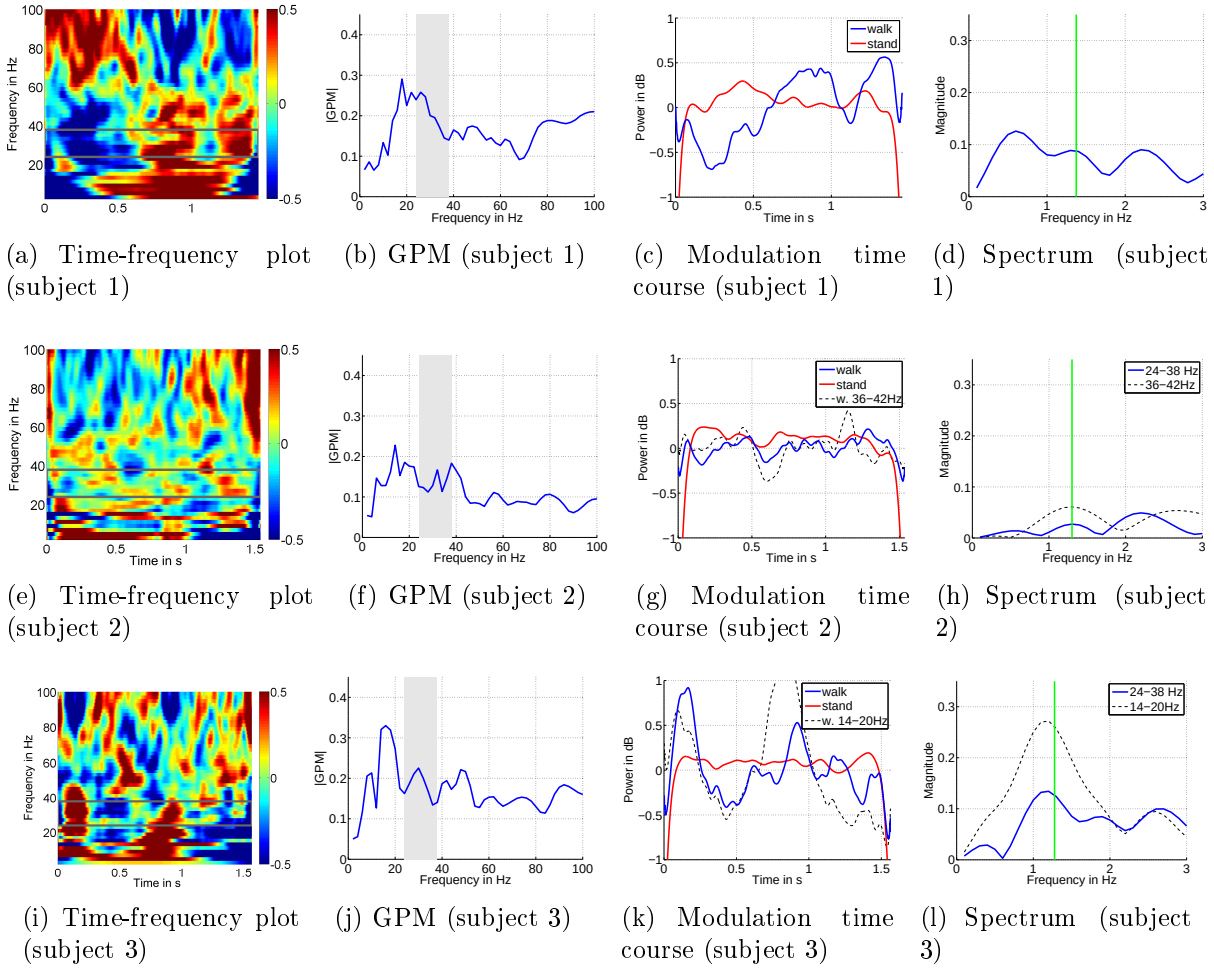


(a) Time-frequency plot (subject 1) (b) GPM (subject 1) (c) Modulation time course (subject 1) (d) Spectrum (subject 1)

(e) Time-frequency plot (subject 2) (f) GPM (subject 2) (g) Modulation time course (subject 2) (h) Spectrum (subject 2)

(i) Time-frequency plot (subject 3) (j) GPM (subject 3) (k) Modulation time course (subject 3) (l) Spectrum (subject 3)

Figure 24: Modulation pattern in a mean gait cycle (subjects 1-3). Top: Mean-free time-frequency representation of average gait cycles, middle: time courses within the frequency band 24-38 Hz, bottom: amplitude spectra of the modulation time courses (blue signals in (d)-(f)).

Subject 1 exhibits a strong modulation pattern between approximately 20 and 50 Hz, as well as the converse modulation in high $\gamma$ frequencies documented in [11] and [18]. However, the pattern is highly asymmetric, which accounts for the most prevalent frequency in the modulation band being lower than the cadence.

In subject 2, the pattern is less pronounced and more noisy. According to figure 24(e) and (f), the modulation is more present in a slightly higher frequency band.
In subject 3, the modulation pattern is pronounced, but slightly skewed, and extends from low frequencies to just above 40 Hz. The converse pattern in higher frequencies is weaker than the low $\gamma$ modulation, and located around 50 Hz.

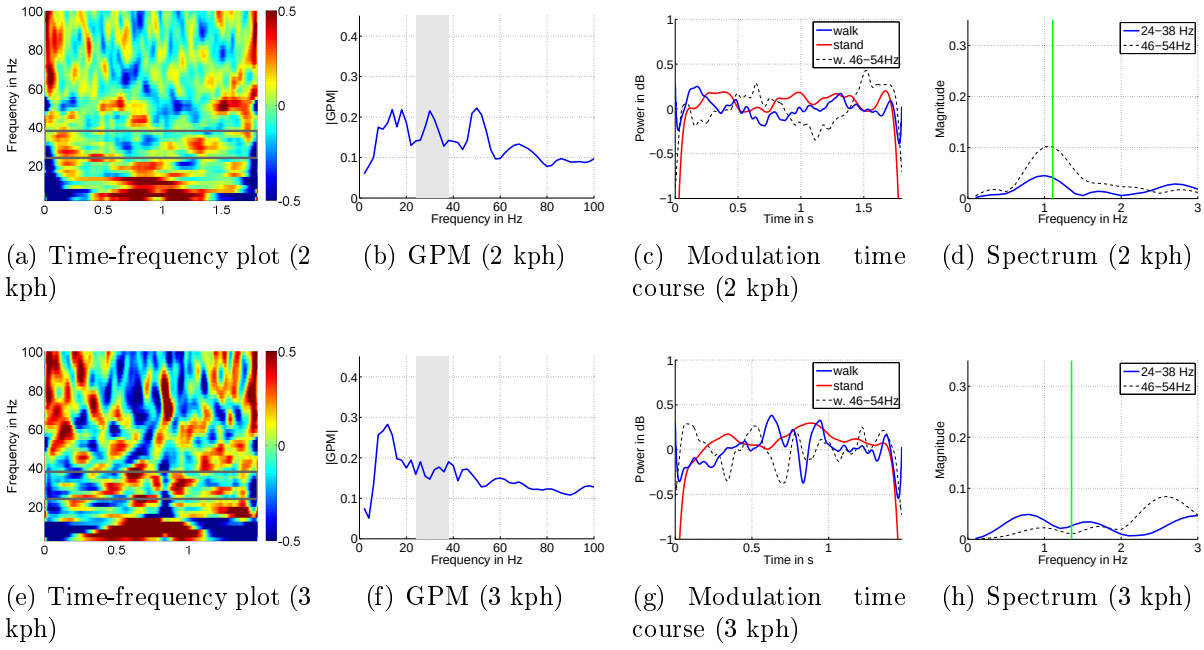


(a) Time-frequency plot (2 kph) (b) GPM (2 kph) (c) Modulation time course (2 kph) (d) Spectrum (2 kph)

(e) Time-frequency plot (3 kph) (f) GPM (3 kph) (g) Modulation time course (3 kph) (h) Spectrum (3 kph)

Figure 25: Modulation patterns in a mean gait cycle (subject 4). Left: Mean-free time-frequency representation of average gait cycles, middle: time courses within the frequency band 24-38 Hz, right: amplitude spectra of the modulation time courses (blue signals in (b),(e)).

Figure 25 illustrates the modulation patterns in subject 4 during walking at two different speeds, 2 kph and 3 kph. While in the slower condition, a weak but discernible modulation pattern is exhibited, accompanied by a converse modulation in a narrow band centered around 50 Hz, the faster condition does not show convincing patterns.
The modulation around 50 Hz is also dominant in subjects 5 and 6, at both speeds, as can be seen in figure 26 and 27. For subjects 5 and 6, the experiment was performed at the treadmill speeds 1.5 kph, and 2 kph.

In the slower condition of subject 5, the low $\gamma$ modulation is disturbed by "noise", but

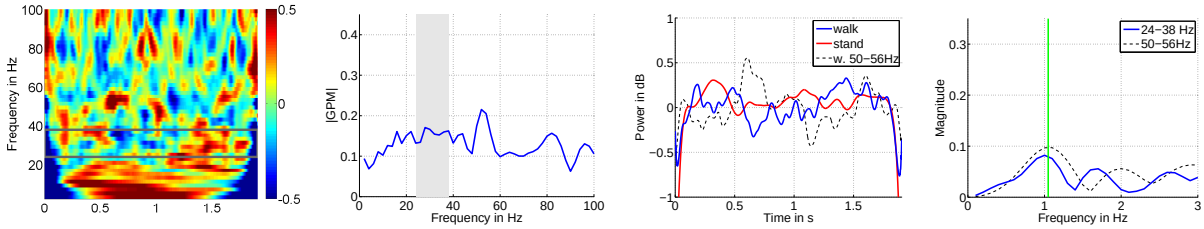


(a) Time-frequency plot (1.5 kph) (b) GPM (1.5 kph) (c) Modulation time course (1.5 kph) (d) Spectrum (1.5 kph)

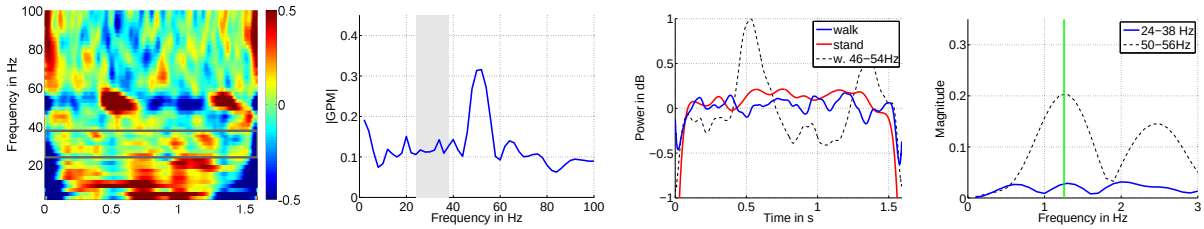


(e) Time-frequency plot (2 kph) (f) GPM (2 kph) (g) Modulation time course (2 kph) (h) Spectrum (2 kph)

Figure 26: Modulation patterns in a mean gait cycle (subject 5). Left: Mean-free time-frequency representation of average gait cycles, middle: time courses within the frequency band 24-38 Hz, right: amplitude spectra of the modulation time courses (blue signals in (b),(e)).

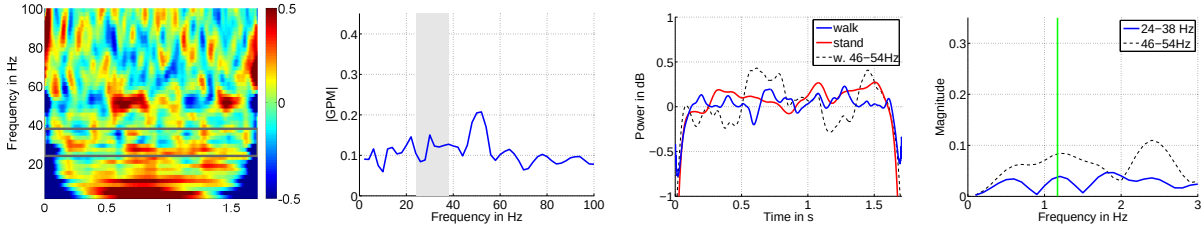


(a) Time-frequency plot (1.5 kph) (b) GPM (1.5 kph) (c) Modulation time course (1.5 kph) (d) Spectrum (1.5 kph)

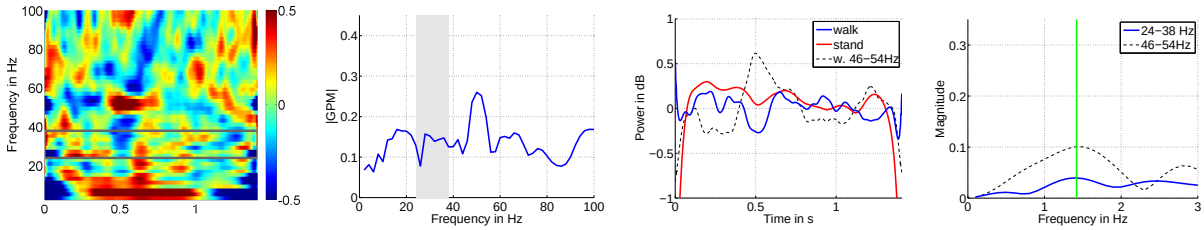


(e) Time-frequency plot (2 kph) (f) GPM (2 kph) (g) Modulation time course (2 kph) (h) Spectrum (2 kph)

Figure 27: Modulation patterns in a mean gait cycle (subject 6). Left: Mean-free time-frequency representation of average gait cycles, middle: time courses within the frequency band 24-38 Hz, right: amplitude spectra of the modulation time courses (blue signals in (b),(e)).

detectable. In the faster condition, on the other hand, it is almost non-existent. The same can be said for the slower condition of subject 6, while in the faster condition, the

modulation is smoother, but somewhat irregular.

# 4 Discussion

The main objective of this thesis - implementing a framework to estimate the gait state and the gait cadence from EEG in an online setup - was achieved. The developed parameter estimation process was validated on EEG recorded during Lokomat walking, and applied in online treadmill experiments. The framework produces real-time output every five seconds.
The length of trial segments was generously set to said five seconds to allow for some averaging, in order to combat the low SNR (Signal to Noise Ratio). Depending on treadmill speed and stride length, one trial segment contains approximately 2 to 3.5 gait cycles, i.e. 4 to 7 modulation periods. In principle, the design of the system would permit the use of overlapping segments to produce more frequent output; however, this was eventually rejected because of the computational effort of the processing.

In phase 1, an effort was made to design a skinny system, avoiding any unnecessary or inefficient computations. All computations were performed only on the amount of data necessary for feature computation, i.e. the frequencies within the chosen $\mu$, $\beta$ and low $\gamma$ frequency bands and the source vertices included in the region of interest.

The implementation of the PSCA artifact correction method necessitated rigorous changes. To capture the characteristics of the artifactual component to remove, a sufficiently large frequency and spatial range has to be covered. Therefore, all steps up to the computation of the relative power spectrum had to be conducted using the whole source space. The chosen frequency range was 2-100 Hz.
The time-frequency decomposition was then performed in the significantly smaller channel space rather than in the source space, and transformed to the source space as complex signals, before computing the magnitude.
In addition, the raw EEG signals were downsampled to half the sample rate (250 Hz). After the computation of the Wavelet decomposition (for which a minimum sample rate of 200 Hz was necessary), the signals were further downsampled by a factor of 4 (61.5 Hz). The highest frequency of interest at this point is, by definition, 3 Hz, since this was set as the upper boundary of the modulation frequency estimation, and the features for the gait state identification do not contain temporal information.

Although the results of the offline simulation presented here were computed with a sample rate of 500 Hz, the downsampling procedure was tested on these data. No distorting impact on the results was found.

## 4.1 Offline Simulation vs. Online Experiments

The results of the offline simulations performed on data recorded during Lokomat walking in 10 subjects demonstrate the plausibility of estimating parameters identified by the gait model put forth in [9] in real time. Performance in the online treadmill experiments was less robust - both the gait state classification and cadence estimation were rather volatile in the 6 subjects. The inter-subject variability was greater than in the Lokomat data set.

Several important points must be taken into account when comparing the results. First of all, the online experiments were performed with different EEG recording equipment and, more importantly, using a more sparse sensor setup (64 electrodes instead of 120). On the other hand, the mobile eego$^{TM}$sports setup (used in the treadmill experiments) may be less prone to cable swing artifacts, since all electrodes are integrated in the EEG cap and connected to the amplifier, which is carried in a light backpack, via one single cable harness.
For performance reasons, the cortical source space was downsampled to 5000 source vertices for the online experiments - a third of the vertices used in the offline simulations.

Furthermore, there are some inherent differences between robot-assisted walking and walking on a treadmill without guidance.

### 4.1.1 Robot-Assisted Gait vs. Treadmill Walking

Although a Lokomat aims at producing a natural walking movement, [34] and [35] found significant differences in electromyographic and kinematic measurements between free treadmill walking and Lokomat assisted walking.

A treadmill places less restrictions on the subject than a gait orthosis like a Lokomat. The Lokomat provides body weight support, which limits movements of the core and torso, thus reducing the amount of artifacts produced by swaying. Furthermore, the movement sequence of the legs is dictated by the Lokomat to a large degree, with little possibility to deviate from the programmed gait rhythm. This certainly leads to less variability in the gait cadence, and potentially a more stable pattern throughout the experiment. In unguided treadmill walking, on the other hand, the only real constraint is the speed of the treadmill. The subject is not kept from e.g. swaying, changing the stride length or walking in an asymmetrical way.
Analysis of the step durations revealed that in the treadmill subjects, the variance is 1.2-29.9 times larger than in the Lokomat subjects. Two main contributions to the high variance are drifts in the stepping patterns and differences in the stepping frequency in separate runs (at the same treadmill speed) resulting from differences in stride length.

This is hard to control for, and may constitute a problem for the frequency estimation, since a skewed or irrelgular modulation pattern will likely not be recognized.

## 4.2 Classification of the Gait State

In the offline simulation on recordings from Lokomat experiments, all subjects performed well in the state discrimination stage. The results presented above were computed with preset frequency bands for the $\mu$ and $\beta$ features. For some subjects, the accuracy could be slightly embellished by adjusting these bands according to individual ERD peaks.
For some subjects, most notably subject 1, the sensitivity and the specificity diverge considerably. The feature distributions depicted in figure 15 suggest that this happens because a considerable part of the standing distribution overlaps with the walking features, which is more clustered.

In the online treadmill experiments, only two subjects achieved accuracies above 80%, for the second of which the specificity barely superceded 70%. For the other four subjects, the power spectrum of mean gait cycles revealed that the power decrease during movement was weak. In addition, for some of the subjects, the spectral peaks were not aptly covered by the generic frequency bands.
As stated in the introduction, the $\beta$ power decrease and the low $\gamma$ modulation tend to overlap in the frequency dimension. In [18], the sum effect found in the signals (in the relevant frequencies) is presented as an oscillation with the modulating frequency, and a negative offset. In the subjects used for the offline simulation, the negative offset resulting from the suppression of $\beta$ oscillations is large enough not to be disturbed by the modulation. However, the presence of the modulation can be obsserved in subject 5, 8 and 10 (see figures 32, 35 and 37 in the appendix). In subjects 5 and 10, the spectral overlap is only partial, and thus the effect is mainly cosmetic. Subject 8's $\beta$ peak, however, is broad and shallow; the whole modulation is visible.
Averaging across the temporal dimension should get rid of the influence of the modulation on $\beta$ features. However, if the modulation pattern is not symmetrical - which is the case for some online subjects -, the $\beta$ features may be weakened.
In addition to this, in three of the online subjects, the power features changed significantly ($p < 10^{-7}$) between training runs and evaluation runs.

For subjects 1 and 2, accuracies were improved by the revision of the framework. Subject 3, on the other hand, performed worse after the revision. Inspection of the feature distribution in figures 12(c) suggests that the discrimination of the gait states was based on artifacts rather than on ERD, since the amplitudes in the walking condition are higher than in the standing condition. In comparison, according to 18(c), the distribution of

the walking condition was shifted downwards, mainly in the $\beta$ dimension, indicating a reduction of artifactual contributions.

## 4.3 Cadence Estimation from Gait Phase Related Modulations

Evidently, the quality of the estimation results is heavily correlated with the pronouncedness and symmetry of the mean gait cycle patterns, which were published in [9]. Said patterns were reproduced and are documented in the appendix for the 10 subjects included in the offline simulation.
In the case of subjects 2 and 9 of the Lokomat data set, there are distortions in the mean gait cycle patterns. Closer examination leads to the conclusion that the PSCA did not fully remove these artifactual distortions. To which extent this is also taking the same effect on the patterns in single trials remains unclear.
In phase 2, 8 of 10 median estimates are located at the nearest frequency bin to the median true cadence, and in all cases within $\pm$ 1 bin. In 6 subjects, the distribution of squared errors is significantly different between walking and standing.

The online results from the treadmill experiments performed worse in comparison. Overall, there is a high degree of randomness. Modulation patterns were, insofar as they were distinguishable, weak, and sometimes located (partly) outside of the selected frequency band.

For subjects 4, 5 and 6, the estimates for the standing condition curiously exhibited a distribution around a peak frequency, instead of a rather flat spectrum. The results are especially bad in subject 6, where all three conditions yielded the same outcome. The search for possible reasons was inconclusive.

To some extent, the system was expected to perform less robustly during treadmill walking, because of the reasons stated above. To recap, the EEG is likely more polluted by movement artifacts, and, on the other hand, the modulation pattern can be expected to be less stable and pronounced.
The issue of movement artifacts was addressed by measures to minimize them in the first place, as well as with an adapted version of the correction method introduced in [11].

Interestingly, 4 subjects exhibited a pronounced modulation in a frequency band of approximately 10 Hz around 50 Hz. In subjects where a modulation pattern was distinguishable in the low gamma band, this modulation is phase shifted in relation to the low gamma modulation, much like the (broader) high gamma modulations documented in [11] and [18]. This modulation has not been documented before in this form. However, even

though it seems to be more suited for the frequency estimation than the low $\gamma$ modulation feature in this pool of subjects, this would be problematic, because power line artifacts are located in this frequency band.

## 4.4 Artifact Treatment

In experiments involving movement, it is crucial to address the problematic of movement artifacts in an appropriate manner. As a preventive measure to keep the disturbing influences low, subjects were instructed to avoid movements which are non-essential to the walking movement itself, especially head movements.
Since movement artifacts disproportionately affect EEG signals recorded near neck muscles, computing the features from an anatomical region of interest helps reduce the damaging influence, since these EEG signals contribute little to the source signals in the paracentral ROI (compared to other cortical regions), which is distant from the neck.

When strong transient artifacts occur, which elevate the measured signals above a threshold of $200\mu V$, affected trials are rejected.

[11] dealt with artifacts inevitably produced by the walking movement by applying PSCA to source space signals, and discarding the component pertaining to the largest eigenvalue of the covariance matrix in the inverse operation. This method was adapted for online use.
In order not to blindly discard signal components, the PSCA was only applied to a trial if the largest eigenvalue was more than five times as high as the second largest one (rule of thumb).

In subject 3 of the online experiments, the EEG was heavily polluted by artifacts. Referring to figure 18(c), the separation of feature distributions by the classifier seems to be artifact-based, since the amplitude of walking trials tends to be higher than that of standing trials, which contradicts the core property of ERD. In comparison, in phase 2 the walking distribution was shifted. This could indicate the removal of artifacts from the signals.
To some extent, the downward shift in the distribution of walking features is also observable in several of the other subjects (of both data sets).

## 4.5 Conclusion

According to a simplified gait model consisting of two elements - namely the gait state and the gait cadence -, features were defined identifying said elements. From the defined features, the gait state and cadence were estimated from live EEG and output in real time

(in five-second intervals).
The presented framework was tested on offline EEG recordings from a Lokomat walking experiment, and applied in online treadmill experiments. Furthermore, an online artifact correction method was implemented.
The results of development phase 1 were successfully submitted to the 2016 IEEE International Conference on Systems, Man, and Cybernetics (SMC) ([21]).

While there is still work to be done to improve the estimation performance, the basic framework was successfully set up, and shown to work in real time, as desired.

Moving on from this point, there are several issues worth exploring more extensively. First of all, the results of offline simulations on data from Lokomat-assisted gait and online treadmill experiments posed questions concerning the comparability of robot-assisted walking and treadmill walking. These open questions may well be consequential for the estimation performance, since deviations in the cortical representation of gait between the two modalities may necessitate an adaptation of the parameter model. To date, I am not aware of publications comparing those two conditions with respect to cortical activity. Experiments specifically targeted at a comprehensive comparison of the two walking modalities may provide some resolve to these issues.

Concerning the estimation framework more directly, it may be advisable to work with subject-specific frequency bands for the feature computation. This could be done either performing a pre-screening EEG measurement of subjects or possibly using the training data to compute spectral profiles from mean gait cycle patterns. In the latter case, it would be advisable to fill the inevitable waiting period with some useful activity, to keep the subject alert.
In this thesis, there was some (limited) experimentation with walking speeds. Although no conclusive influences on the patterns were found, further investigation might yield valuable insights.

Finally, an in-depth investigation on the efficacy of the PSCA artifact removal method with respect to online EEG would be in order.

# References

[1] Pfurtscheller G, Aranibar A: Event-related cortical desynchronization detected by power measurements of scalp EEG. *Electroencephalogr Clin Neurophysiol* 42: 817–826 (1977)

[2] Pfurtscheller G, Lopes da Silva F H, Event-related EEG/MEG synchronization and desynchronization: basic principles. *Clin Neurophysiol* 110: 1842–1857 (1999)

[3] Crone N E, Miglioretti D L, Gordon B, Sieracki J M, Wilson M T, Uematsu S, Lesser R P: Functional mapping of human sensorimotor cortex with electrocorticographic spectral analysis: I. Alpha and beta event-related desynchronization. *Brain* 121: 2271–2299 (1998a)

[4] Müller G R, Neuper C, Rupp R, Keinrath C, Gerner H J, Pfurtscheller G: Event-related beta EEG changes during wrist movements induced by functional electrical stimulation of forearm muscles in man. *Neurosci Lett* 340: 143–147 (2003)

[5] Miller K J, Leuthardt E C, Schalk G, Rao R P, Anderson N R, Moran D W, Miller J W, Ojemann J G: Spectral changes in cortical surface potentials during motor movement. *J Neurosci* 27: 2424–2432 (2007)

[6] Scherer R, Zanos S P, Miller K J, Rao R P, Ojemann J G: Classification of contralateral and ipsilateral finger movements for electrocorticographic brain-computer interfaces. *Neurosurg Focus* 27: E12 (2009)

[7] Crone N E, Miglioretti D L, Gordon B, Lesser R P: Functional mapping of human sensorimotor cortex with electrocorticographic spectral analysis: II. Event-related synchronization in the gamma band. *Brain* 121: 2301–2315 (1998b)

[8] Wagner J, Solis-Escalante T, Grieshofer P, Neuper C, Müller-Putz G R, Scherer R: Level of participation in robotic-assisted treadmill walking modulates midline sensorimotor EEG rhythms in able-bodied subjects. *Neuroimage* 63 (3): 1203-1211 (2012)

[9] Seeber M, Scherer R, Wagner J, Solis-Escalante T, Müller-Putz G R: EEG beta suppression and low gamma modulation are different elements of human upright walking. *Front Hum Neurosci* 8: 485 (2014)

[10] Gwin J T, Gramann K, Makeig S, Ferris D P: Electrocortical activity is coupled to gait cycle phase during treadmill walking. *Neuroimage* 54 (2): 1289–1296 (2011)

[11] Seeber M, Scherer R, Wagner J, Solis-Escalante T, Müller-Putz G R: High and low gamma EEG oscillations in central sensorimotor areas are conversely modulated during the human gait cycle. *Neuroimage* 112: 318-326 (2015)

[12] Baillet S, Mosher J C, and Leahy R M: Electromagnetic brain mapping. *IEEE Signal Process Mag* 18: 14–30 (2001)

[13] Michel C M, Murray M M, Lantz G, Gonzalez S, Spinelli L, Grave de Peralta R: EEG source imaging. *Clin Neurophysiol* 115: 2195–2222 (2004)

[14] Darvas F, Pantazis D, Kucukaltun-Yildirim E, Leahy R M: Mapping human brain function with MEG and EEG: methods and validation. *Neuroimage* 23: S289–S299 (2004)

[15] Michel C M, Murray M M: Towards the utilization of EEG as a brain imaging tool. *Neuroimage* 61:371–385 (2012)

[16] Donner T H, Siegel M: A framework for local cortical oscillation patterns. *Trends Cogn Sci* 15: 191–199 (2011)

[17] Siegel M, Donner T H, Engel A K: Spectral fingerprints of large-scale neuronal interactions. *Nat Rev Neurosci* 13: 121–134 (2012)

[18] Seeber M, Scherer R, Müller-Putz G R: EEG Oscillations Are Modulated in Different Behavior-Related Networks during Rhythmic Finger Movements. J Neurosci 36(46): 11671–11681 (2016)

[19] Seeber M, Wagner J, Scherer R, Solis-Escalante T, Müller-Putz G R: Reconstructing gait cycle patterns from non-invasive recorded low gamma modulations. *Proceedings of the 6th International Brain-Computer Interface Conference* (2014)

[20] Lisi G, Morimoto J: EEG single-trial detection of gait speed changes during treadmill walk. *PLoS One* 10(5): e0125479 (2015)

[21] Hehenberger L, Seeber M, Scherer R: Estimation of gait parameters from EEG source oscillations. *2016 IEEE International Conference on Systems, Man, and Cybernetics* (2016)

[22] Oostenveld R, Praamstra P: The five percent electrode system for high-resolution EEG and ERP measurements. *Clin Neurophysiol* 112(4): 713-719 (2001)

[23] Delorme A, Mullen T, Kothe C, Akalin Acar Z, Bigdely-Shamlo N, Vankov A, Makeig S: EEGLAB, SIFT, NFT, BCILAB, and ERICA: New tools for advanced EEG processing. *Comput Intell Neurosci* 2011 (2011)

[24] Hallez H, Vanrumste B, Grech R, Muscat J, De Clercq W, Vergult A, D'Asseler Y, Camilleri K P, Fabri S G, Van Huffel S, Lemahieu I: Review on solving the forward problem in EEG source analysis. *J Neuroeng Rehabil* 4: 46 (2007)

[25] Tadel F, Baillet S, Mosher J C, Pantazis D, Leahy R M: Brainstorm: A User-Friendly Application for MEG/EEG Analysis. *Comput Intell Neurosci* 2011: 879716 (2011)

[26] Hämäläinen M S, Ilmoniemi R J: Interpreting magnetic fields of the brain: minimum norm estimates. *Med Biol Eng Comput* 32: 35–42 (1994) CrossRef Medline

[27] Pascual-Marqui R D. Standardized low-resolution brain electromagnetic tomography (sLORETA): technical details. Methods Find Exp Clin Pharmacol 24D: 5-12 (2002)

[28] Fuchs M, Wagner M, Kastner J: Boundary element method volume conductor models for EEG source reconstruction. Clin Neurophysiol 112: 1400-1407 (2001)

[29] Dale A, Fischl B, Sereno M I: Cortical surface-based analysis. I. Segmentation and surface reconstruction. *Neuroimage* 9: 179–194 (1999)

[30] Fischl B: FreeSurfer. *Neuroimage* 62: 774–781 (2012)

[31] Gramfort A, Papadopoulo T, Olivi E, Clerc M: OpenMEEG: Opensource Software for Quasistatic Bioelectromagnetics. *Biomed Eng Online* 9:45 (2010)

[32] Kybic J, Clerc M, Abboud T, Faugeras O, Keriven R, Papadopoulo T: A Common Formalism for the Integral Formulations of the Forward EEG Problem. *IEEE Trans Med Imaging* 24: 12-28 (2005)

[33] Morlet J, Arens G, Fourgenau E, Glard D: Wave propagation and sampling theorypart I: complex signal and scattering in multilayered media. *Geophysics* 47(2): 203-221, 1982.

[34] Hidler J M, Wall A E: Alterations in muscle activation patterns during robotic-assisted walking. *Clin Biomech* 20: 184–193 (2005)

[35] Hidler J, Wisman W, Neckel N: Kinematic trajectories while walking within the Lokomat robotic gait-orthosis. *Clin Biomech (Bristol, Avon)* 23: 1251–1259 (2008)

# 5 Appendix

## 5.1 Mean Gait Cycle Patterns of Lokomat Dataset

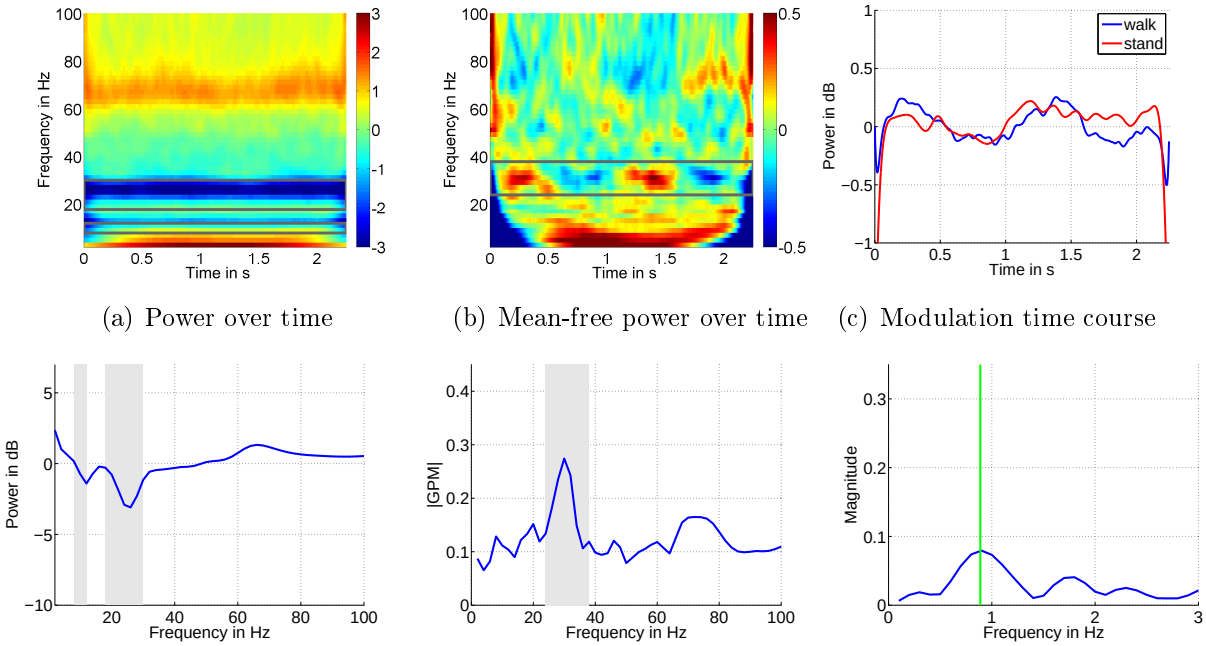


(a) Power over time (b) Mean-free power over time (c) Modulation time course

(d) Power spectrum (e) GPM spectrum (f) Modulation amplitdue spectrum

Figure 28: Mean gait cycle patterns of subject 1 (Offline simulation)

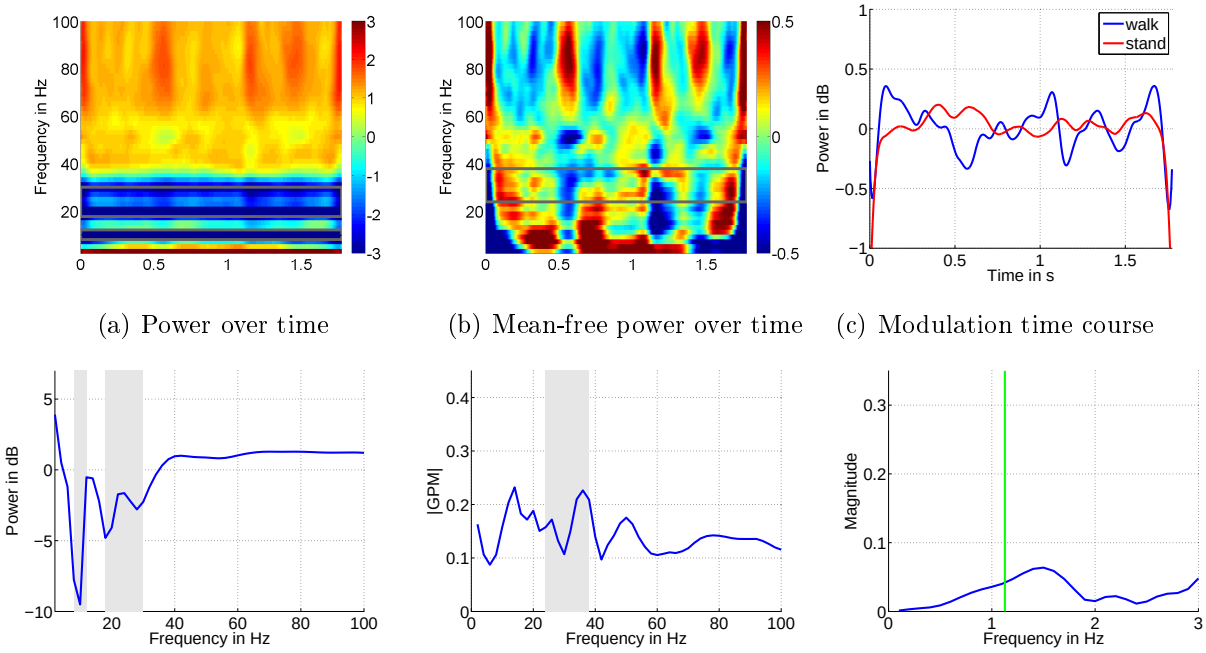


(a) Power over time (b) Mean-free power over time (c) Modulation time course

(d) Power spectrum (e) GPM spectrum (f) Modulation amplitdue spectrum

Figure 29: Mean gait cycle patterns of subject 2 (Offline simulation)

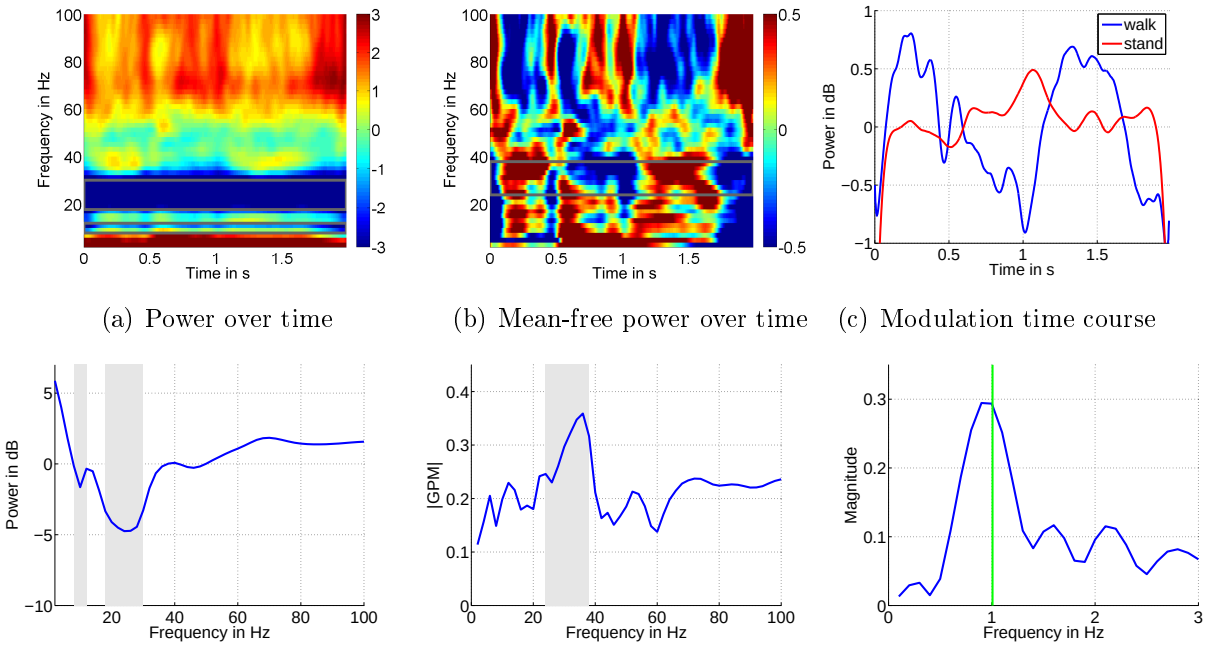


(a) Power over time (b) Mean-free power over time (c) Modulation time course

(d) Power spectrum (e) GPM spectrum (f) Modulation amplitdue spectrum

Figure 30: Mean gait cycle patterns of subject 3 (Offline simulation)

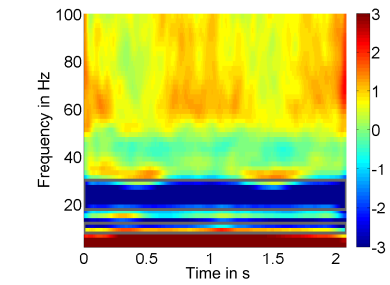


(a) Power over time

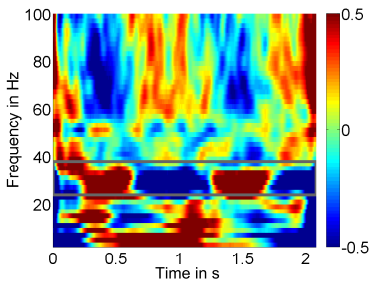


(b) Mean-free power over time

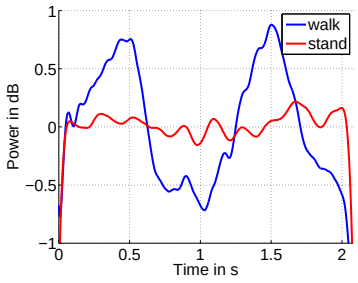


(c) Modulation time course

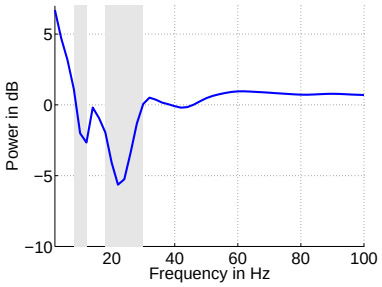


(d) Power spectrum

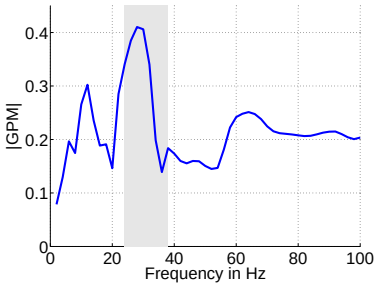


(e) GPM spectrum

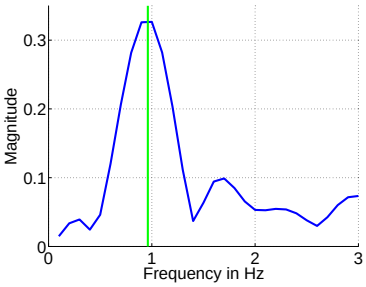


(f) Modulation amplitdue spectrum

Figure 31: Mean gait cycle patterns of subject 4 (Offline simulation)

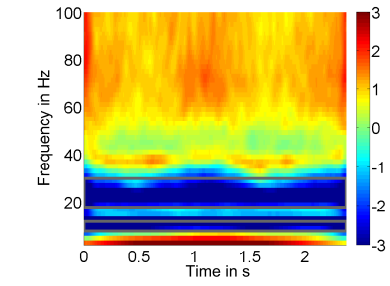


(a) Power over time

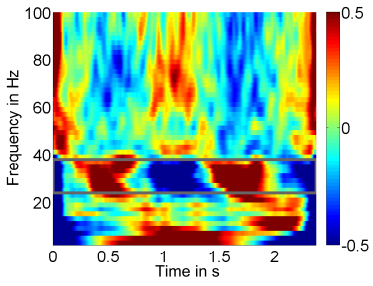


(b) Mean-free power over time

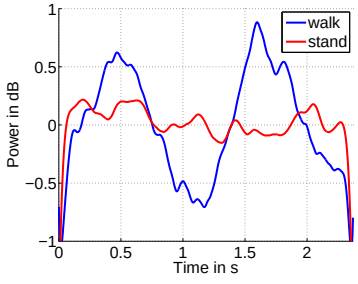


(c) Modulation time course

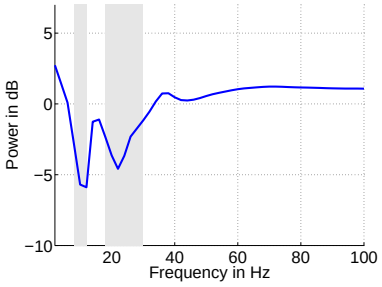


(d) Power spectrum

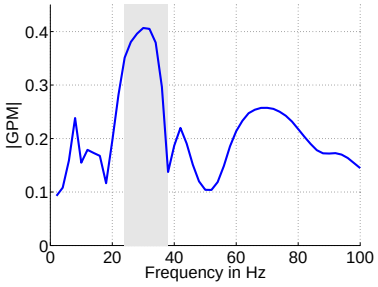


(e) GPM spectrum

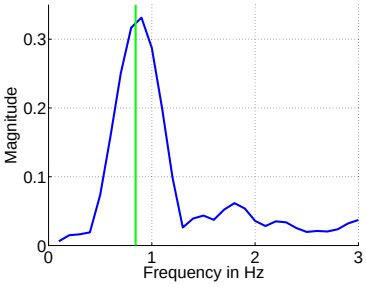


(f) Modulation amplitdue spectrum

Figure 32: Mean gait cycle patterns of subject 5 (Offline simulation)

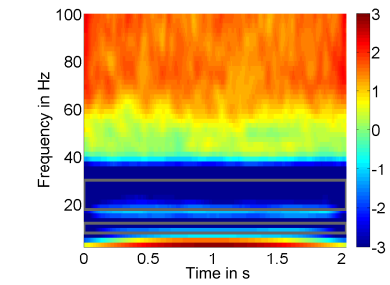


(a) Power over time

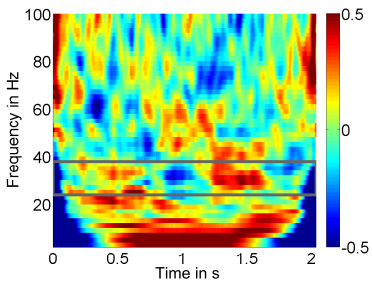


(b) Mean-free power over time

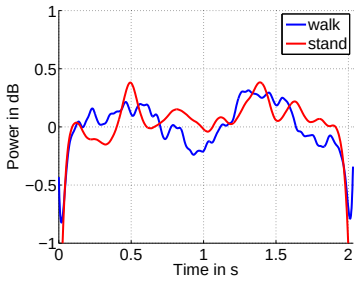


(c) Modulation time course

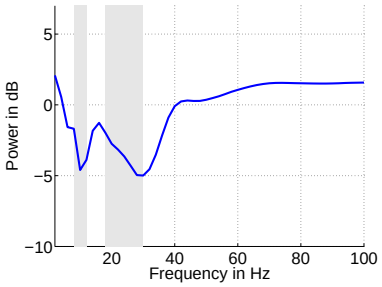


(d) Power spectrum

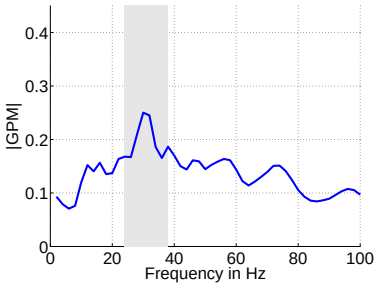


(e) GPM spectrum

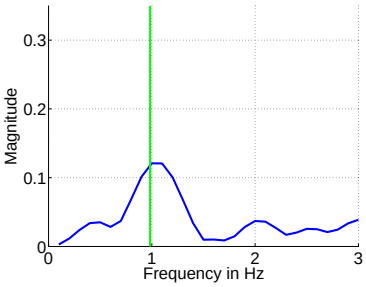


(f) Modulation amplitdue spectrum

Figure 33: Mean gait cycle patterns of subject 6 (Offline simulation)

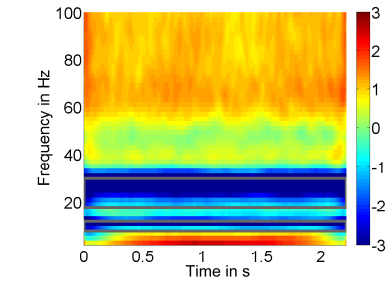


(a) Power over time

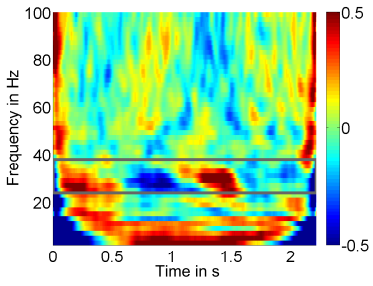


(b) Mean-free power over time

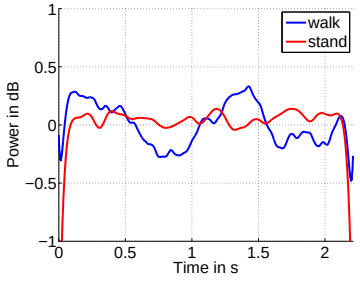


(c) Modulation time course

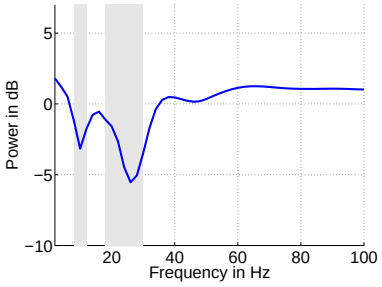


(d) Power spectrum

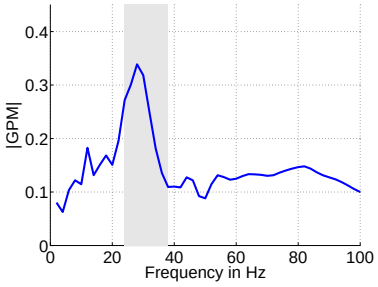


(e) GPM spectrum

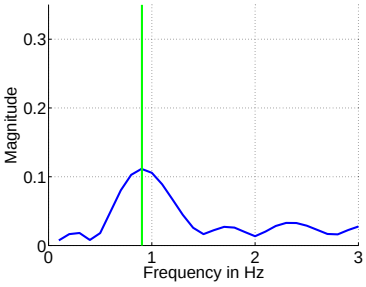


(f) Modulation amplitdue spectrum

Figure 34: Mean gait cycle patterns of subject 7 (Offline simulation)

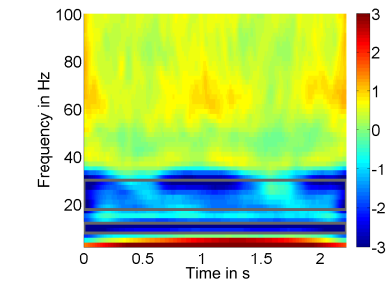


(a) Power over time

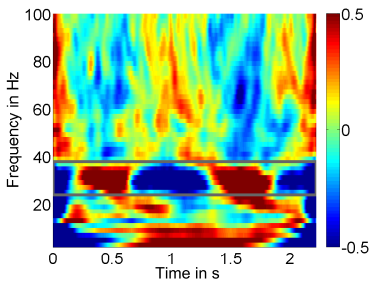


(b) Mean-free power over time

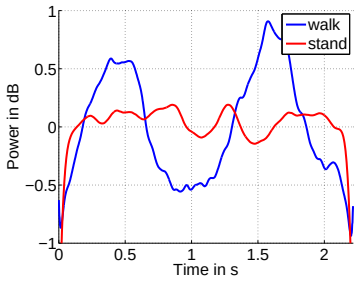


(c) Modulation time course

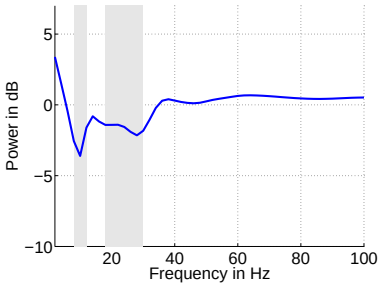


(d) Power spectrum

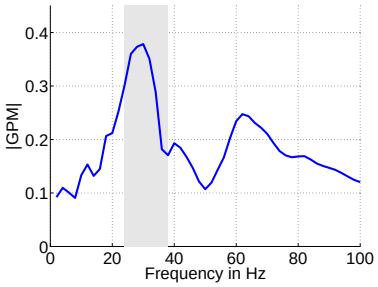


(e) GPM spectrum

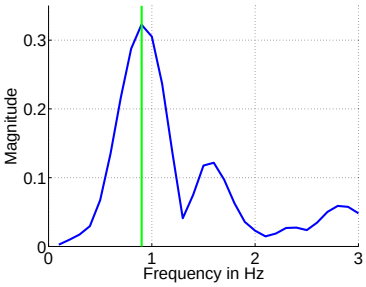


(f) Modulation amplitdue spectrum

Figure 35: Mean gait cycle patterns of subject 8 (Offline simulation)

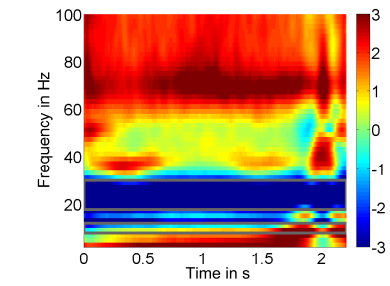


(a) Power over time

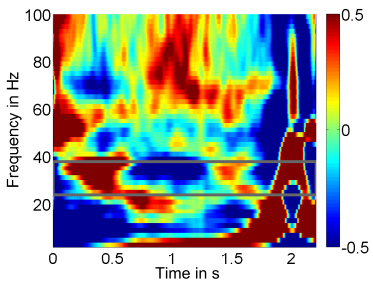


(b) Mean-free power over time

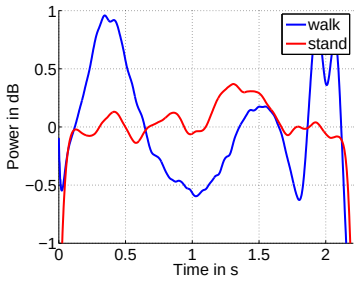


(c) Modulation time course

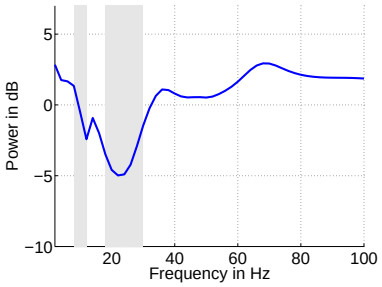


(d) Power spectrum

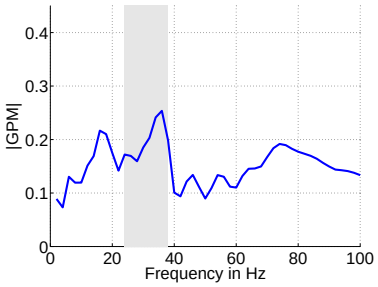


(e) GPM spectrum

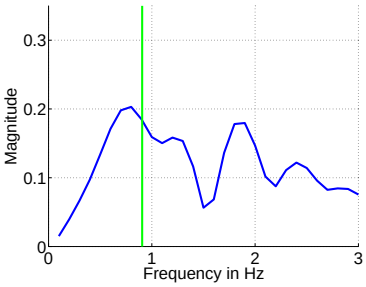


(f) Modulation amplitdue spectrum

Figure 36: Mean gait cycle patterns of subject 9 (Offline simulation)

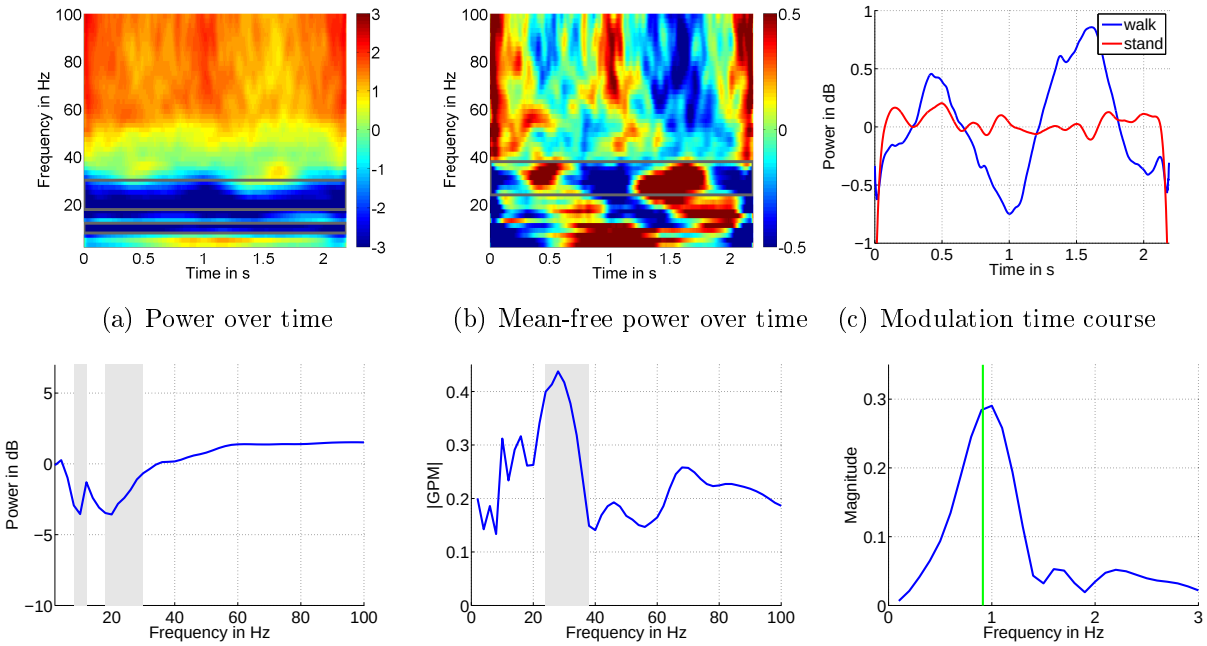


(a) Power over time (b) Mean-free power over time (c) Modulation time course

(d) Power spectrum (e) GPM spectrum (f) Modulation amplitdue spectrum

Figure 37: Mean gait cycle patterns of subject 10 (Offline simulation)

## 5.2 Gait Cadence Estimation with Subject-Specific Frequency Bands

For subject 1, adjusting the modulation frequency band has no effect.

The following figures are structured as follows:
(a) panels: Frequency estimation results, presented as in section 3.
(b) panels: TF plots of zero-mean relative power. Subject-specific modulation bands are marked by gray boxes.
(c) panels: GPM measure (magnitude) across frequency spectrum. Modulation bands are marked by gray shadowed areas.
Modulation frequency bands and treadmill speeds are specified in the captions.

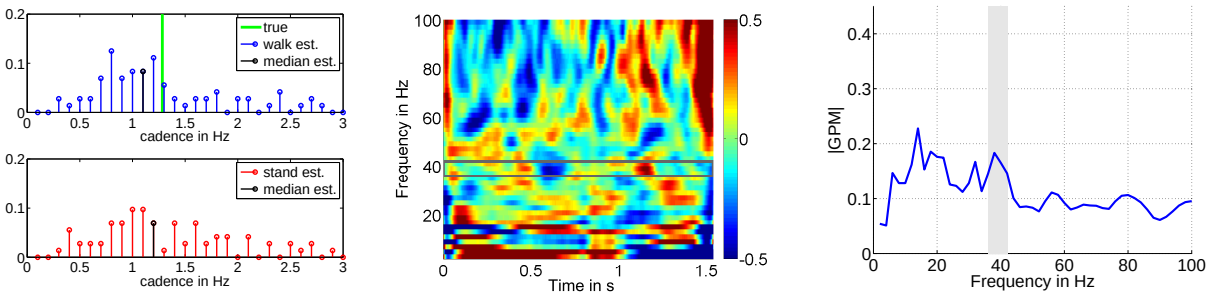


(a) (b) (c)

Figure 38: Cadence estimation results with subject-specific modulation frequency band (subject 2). f = 36-42 Hz. Treadmill speed: 2.4 kph

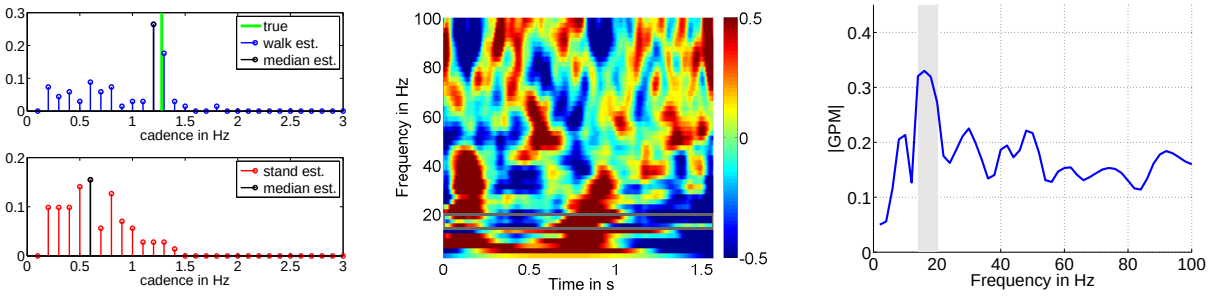


(a) (b) (c)

Figure 39: Cadence estimation results with subject-specific modulation frequency band (subject 3). f = 14-20 Hz. Treadmill speed: 2.4 kph

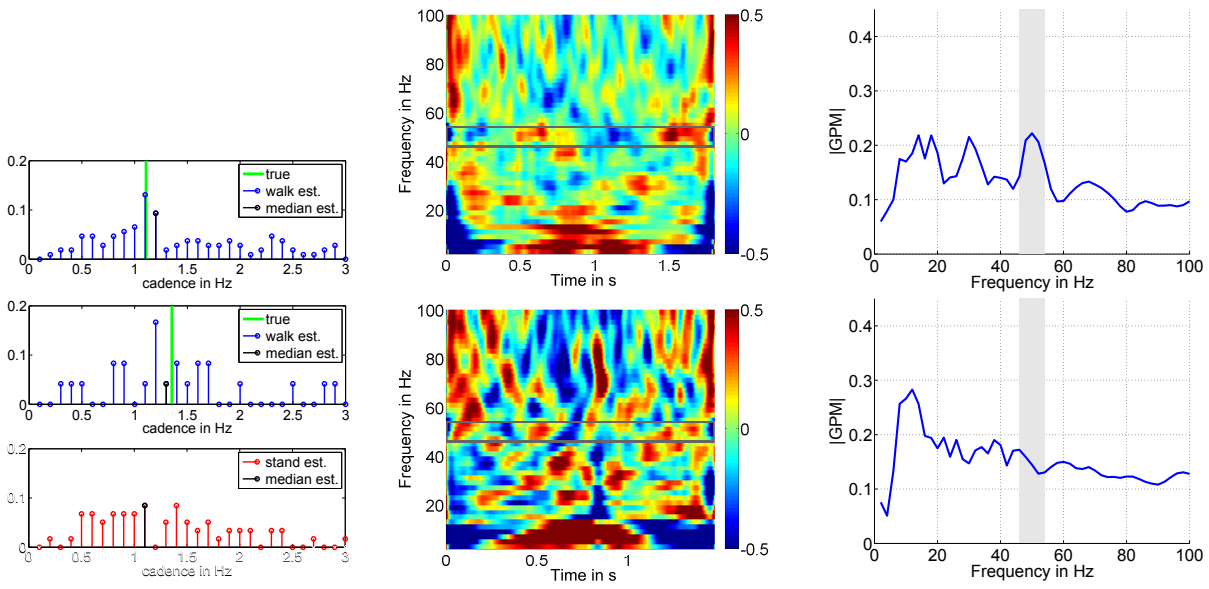


(a) (b) (c)

Figure 40: Cadence estimation results with subject-specific modulation frequency band (subject 4). f = 46-54 Hz. Treadmill speed: 2kph (top), 3kph (middle)

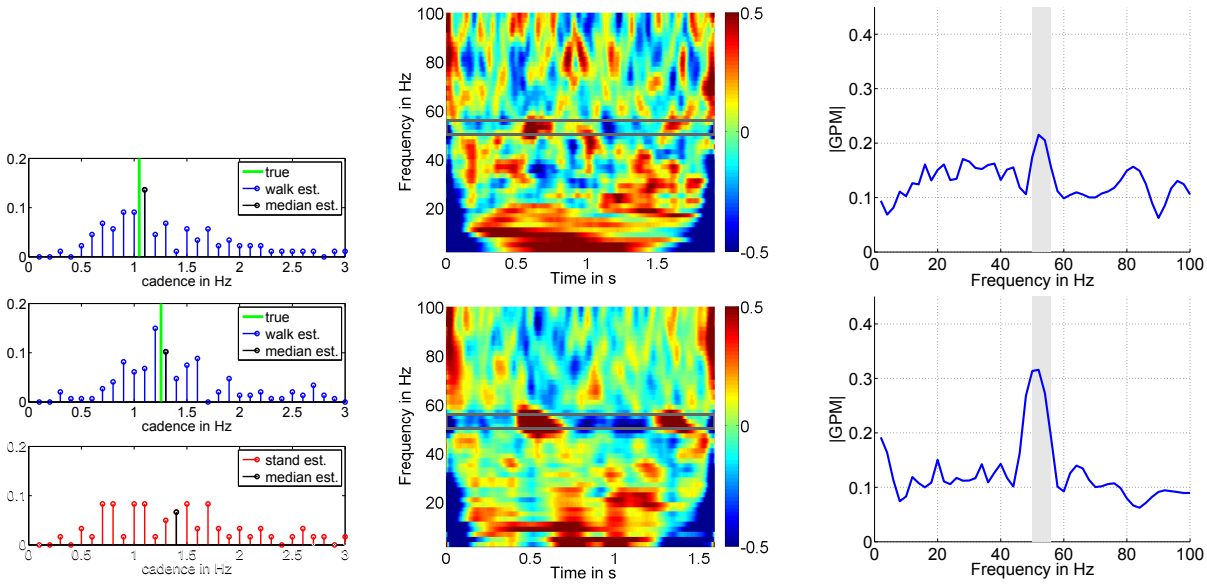


(a) (b) (c)

Figure 41: Cadence estimation results with subject-specific modulation frequency band (subject 5). f = 50-56 Hz. Treadmill speed: 1.5kph (top), 2kph (middle)

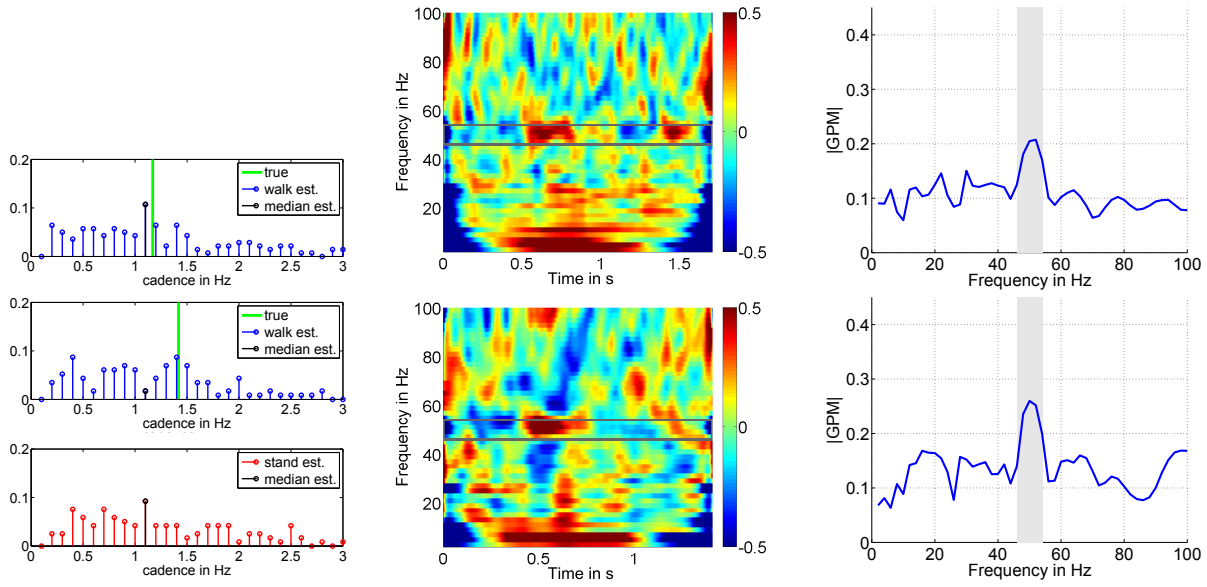


(a) (b) (c)

Figure 42: Cadence estimation results with subject-specific modulation frequency band (subject 6). f = 46-54 Hz. Treadmill speed: 1.5kph (top), 2kph (middle)